

AD-A169 057

FINITE ELEMENT ANALYSES OF SHEAR LOCALIZATION IN RATE  
AND TEMPERATURE DEP. (U) BROWN UNIV PROVIDENCE RI DIV  
OF ENGINEERING J LEMONDS ET AL. MAY 86 ARO-22306.6-EB

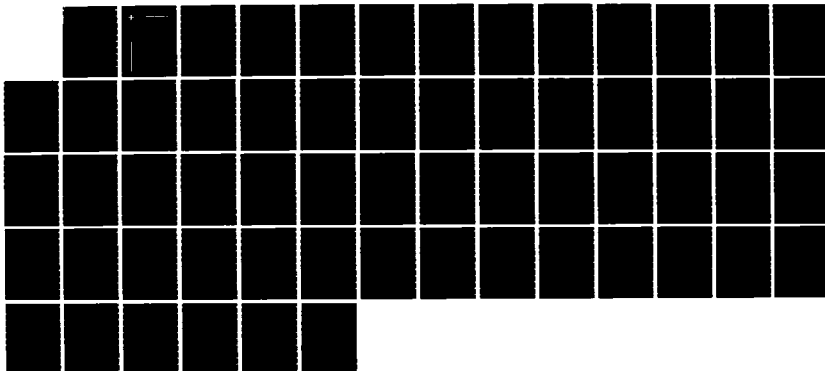
1/1

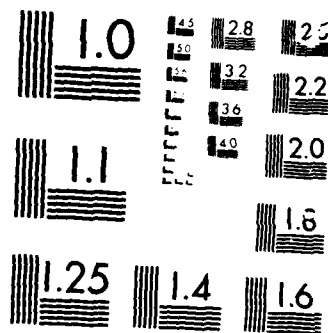
UNCLASSIFIED

DAG29-85-K-0003

F/B 20/11

NL





MICROCOPY

20193



**Brown University**  
DIVISION OF ENGINEERING  
PROVIDENCE, R.I. 02912

2

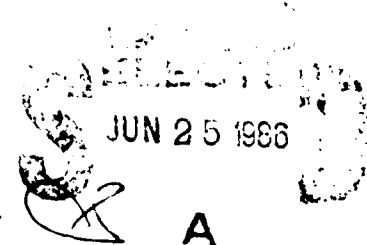
AD-A169 057

FINITE ELEMENT ANALYSES OF SHEAR  
LOCALIZATION IN RATE  
AND TEMPERATURE DEPENDENT SOLIDS

by

J. LeMonds and A. Needleman  
Division of Engineering  
Brown University  
Providence, R.I. 02912

OTIC FILE COPY



This document has been approved  
for public release and sale; its  
distribution is unlimited.

2

**FINITE ELEMENT ANALYSES OF SHEAR  
LOCALIZATION IN RATE  
AND TEMPERATURE DEPENDENT SOLIDS**

by

**J. LeMonds and A. Needleman  
Division of Engineering  
Brown University  
Providence, R.I. 02912**

10

**Army Research Office Report  
No. DAAG 29-85-K-0003/4**

**May, 1986**

UNCLASSIFIED

SECURITY CLASSIFICATION OF THIS PAGE (When Data Entered)

REPORT DOCUMENTATION PAGE		READ INSTRUCTIONS BEFORE COMPLETING FORM
1. REPORT NUMBER <b>ARO 22306.6-E6</b>	2. GOVT ACCESSION NO. <b>AD N7A 169057</b>	3. RECIPIENT'S CATALOG NUMBER <b>N/A</b>
4. TITLE (and Subtitle) "Finite Element Analyses of Shear Localization in Rate and Temperature Dependent Solids"		5. TYPE OF REPORT & PERIOD COVERED <b>Technical</b>
		6. PERFORMING ORG. REPORT NUMBER
7. AUTHOR(s) <b>J. LeMonds and A. Needleman</b>		8. CONTRACT OR GRANT NUMBER(s) <b>DAAG 29-85-K-0003/3</b>
9. PERFORMING ORGANIZATION NAME AND ADDRESS <b>Division of Engineering Brown University Providence, RI 02912</b>		10. PROGRAM ELEMENT, PROJECT, TASK AREA & WORK UNIT NUMBERS <b>N/A</b>
11. CONTROLLING OFFICE NAME AND ADDRESS <b>U. S. Army Research Office Post Office Box 12211 Research Triangle Park, NC 27709</b>		12. REPORT DATE <b>May, 1986</b>
		13. NUMBER OF PAGES <b>55</b>
14. MONITORING AGENCY NAME & ADDRESS (if different from Controlling Office)		15. SECURITY CLASS. (of this report) <b>Unclassified</b>
		15a. DECLASSIFICATION/DOWNGRADING SCHEDULE
16. DISTRIBUTION STATEMENT (of this Report)  <b>Approved for public release; distribution unlimited.</b>		
17. DISTRIBUTION STATEMENT (of the abstract entered in Block 20, if different from Report)  <b>NA</b>		
18. SUPPLEMENTARY NOTES  The view, opinions, and/or findings contained in this report are those of the author(s) and should not be construed as an official Department of the Army position, policy, or decision, unless so designated by other documentation.		
19. KEY WORDS (Continue on reverse side if necessary and identify by block number) <b>Shear Bands Shear Localization Thermoplastic Instability Thermal Softening</b>		
20. ABSTRACT (Continue on reverse side if necessary and identify by block number)  The effects of strain hardening, strain rate sensitivity, thermal softening, heat conduction and the imposed strain rate on the shear localization process in plane strain compression are examined. The deformation, stress and temperature fields are computed in an infinite solid which contains a periodic rectangular array of inhomogeneities. The inhomogeneities give rise to non-uniform deformation fields which, under certain conditions, may localize in the form of a shear band. Boundary conditions are prescribed such that the resulting fields possess		

FINITE ELEMENT ANALYSES OF SHEAR LOCALIZATION IN RATE  
AND TEMPERATURE DEPENDENT SOLIDS

by

J. LeMonds

and

A. Needleman  
Division of Engineering  
Brown University  
Providence, RI 02912

ABSTRACT

The effects of strain hardening, strain rate sensitivity, thermal softening, heat conduction and the imposed strain rate on the shear localization process in plane strain compression are examined. The deformation, stress and temperature fields are computed in an infinite solid which contains a periodic rectangular array of inhomogeneities. The inhomogeneities give rise to non-uniform deformation fields which, under certain conditions, may localize in the form of a shear band. Boundary conditions are prescribed such that the resulting fields possess periodicity with respect to the inhomogeneity distribution. In this manner, attention may be confined to a rectangular region of the solid which surrounds a single inhomogeneity. Full two-dimensional analyses are performed within the context of a viscoplasticity theory which, in the rate independent limit, corresponds to flow theory with combined isotropic and kinematic hardening. Full account is taken of finite strain and rotation effects, but attention is confined to quasi-static loading. The initiation and propagation of shear bands is examined for the bounding theories of isotropic and kinematic hardening. The predicted response depends significantly on the multi-axial hardening characterization of the solid.



AND

1

1

7-1

## 1. INTRODUCTION

Shear bands frequently accompany the large plastic straining of materials. The large localized strains in a shear band often precipitate fracture. When shear bands do not lead to fracture, the localized shearing greatly affects subsequent plastic deformation. Hence, shear bands have a dual significance: as a precursor to fracture and as a mechanism of large strain plastic deformation. In metals subject to high rates of loading, shear bands can form as the result of a thermomechanical instability. The same metal may also undergo shear localization at very low strain rates, where thermal effects are negligible, with some other mechanism causing the observed localization.

The important role of thermal softening in triggering shear band formation at high rates of deformation was recognized by Zener and Hollomon [1]. Experimental investigations of thermal softening induced shear bands have been directed toward microstructural features contributing to and resulting from localization and to measurements of the strain and temperature conditions at which the bands form, Rogers [2], Wright and Batra [3], Moss and Pond [4], Costin et al. [5] and Hartley [6]. Analytical and numerical studies have generally focussed on conditions for instability in simple shearing deformations, Argon [7], Clifton [8], Recht [9], Culver [10], Backman and Finnegan [11], Merzer [12], Fressengeas and Molinari [13], Olsen, Mescall and Azrin [14], Wu and Freund [15] and Shawki [16]. These theoretical studies have elucidated the relative roles of thermal softening, strain hardening and strain rate sensitivity on shear localization in circumstances where the onset of localization does not involve a substantial change in stress state.

Shear band instabilities are also observed at low rates where thermal softening is not significant and, furthermore, in circumstances where there is no evidence for material softening due to progressive rupture on the microscale, Chang and Asaro [17], Anand and Spitzig [18], Larsson et al. [19]. Under isothermal conditions and when microrupture effects are absent, a key feature of plastic material response for shear localization is the yield surface vertex structure implied by the discrete nature of crystallographic slip, Rice [20], Needleman and Rice [21], Asaro [22], Tvergaard et al. [23] and Larsson et al. [19]. In this context the significance of a yield surface vertex lies in the reduced stiffness to a change in loading path.

For rate dependent constitutive relations, a flow potential surface vertex is ruled out on quite general grounds, Rice [24]. However, Tvergaard [25] and Hutchinson and Tvergaard [26] have shown that a solid having a smooth yield surface but with a high curvature (relative to the isotropic hardening surface) at the current loading point can give predictions of necking and shear band instabilities in line with those based on a corner theory of plasticity.

In this investigation, we analyze the development of localization from a small internal material inhomogeneity in a situation where localization involves a considerable change in loading path. The formulation incorporates the effects of thermal softening, strain hardening, strain rate sensitivity and heat conduction. Full account is taken of finite geometry changes, but inertial effects are neglected. We confine attention to a range of strain rates, from say  $10^{-3} \text{ sec}^{-1}$  to  $10^3 \text{ sec}^{-1}$ , where material rate sensitivity is the main time effect and higher strain rates where inertial effects play an important role are excluded from consideration. The particular boundary value problem analyzed is plane strain compression of a block of material containing a doubly periodic array of inhomogeneities. The doubly periodic symmetry permits the problem



for the entire array to be reduced to a boundary value problem for one square cell. No heat flux is permitted between cells so that there is an overall adiabatic response. However, within each cell heat conduction is accounted for.

Previous analyses of shear localization at internal inhomogeneities have been carried out for rate independent solids deforming isothermally by Abeyaratne and Triantafyllidis [27] for plane strain and by Freund, Wu and Touloukian [28] for anti-plane shear. Abeyaratne and Triantafyllidis [27] confined attention to quasi-static deformations while in Freund, Wu and Touloukian [28] full account was taken of material inertia.

Here, we present results for both isotropically and kinematically hardening solids. A particular focus of our work is the influence of flow potential surface curvature on the tendency for localization at various strain rates and we use a kinematic hardening flow rule to model a "rounded vertex." This use of kinematic hardening theory is intended for loading paths that do not involve extreme deviations from proportional loading and is quite distinct in focus from the use of kinematic hardening as a model for Bauschinger effects. Our results exhibit the transition from plastic flow property dominated shear band localization at low rates to thermal softening dominated localization at higher strain rates, with the details of this transition depending sensitively on the description of the flow potential surfaces.

## 2. FIELD EQUATIONS

### 2.1 Incremental Principle of Virtual Work

The governing equations for the finite element discretization of the momentum balance equation are based on a Lagrangian convected coordinate system. This approach has been used extensively in a variety of contexts involving finite deformation analysis, e.g., Needleman [29], Tvergaard [30], and for rate dependent constitutive relations by Peirce, Asaro and Needleman [31]. Some essential features of the formulation will be outlined here.

The reference configuration for the Lagrangian formulation corresponds to the initial unstressed state with the material points identified by the Cartesian coordinates  $x^i$ . In the current deformed state, the material points are at  $x^i + u^i$  where  $u^i$  are the components of the displacement vector on the referential base vectors and  $F = \partial(x+u)/\partial x$  is the deformation gradient.

A current state of approximate equilibrium is known at time  $t$ , and the incremental principle of virtual work is used to compute the time rate of change of the field variables for a time increment  $\Delta t$ . Under plane strain conditions with body forces neglected, this principle may be expressed as

$$\int_A \dot{n}^{ij} \delta F_{ji} dA = \int_S \dot{T}^i \delta u_i dS + \frac{1}{\Delta t} \left[ \int_S T^i \delta u_i dS - \int_A n^{ij} \delta F_{ji} dA \right] \quad (2.1)$$

where  $A$  and  $S$  denote the interior and the boundary of the body in the reference configuration, respectively, and  $(\dot{\phantom{x}})$  indicates the material time derivative. The components  $n^{ij}$  are the contravariant components of the nominal stress tensor;  $T^i$  are the components of the nominal traction vector, given by  $T^i = n^{ji} v_j$ , where  $v$  is the unit normal to the boundary in the reference configuration; and  $F_{ij}$  are the covariant components of the deformation gradient; the components of each of these tensors being on the reference base vectors. The term in brackets on the

right side of (2.1) serves to correct slight deviations from equilibrium which result from incremental time integration.

## 2.2 Balance of Energy

The principle of energy balance requires that the time rate of change of energy (internal plus kinetic) be equal to the power input arising from internal and surface forces and heating. The following simplifying assumptions are made: 1) the rate of change of internal energy may be expressed as  $\rho c_p \partial T / \partial t$  where  $\rho$  is the mass density and  $c_p$  is the specific heat at constant pressure; 2) Fourier's law of heat conduction applies - the heat flux is proportional to the temperature gradient, with the constant of proportionality being the thermal conductivity; 3) the fraction of plastic stress work which is converted to heat is  $\chi$ , where  $\chi$  is in the range of 0.85 to 0.95 for many metals (Taylor and Quinney [32]). These assumptions allow the referential form of the energy balance equation to be written as

$$\rho c_p \frac{\partial T}{\partial t} = \nabla_0 \cdot (k \nabla_0 T) + \chi \tau : d^p \quad (2.2)$$

where  $\nabla_0$  represents the gradient with respect to the coordinates in the reference configuration, and  $d^p$  is the plastic part of the rate of deformation tensor. The rate of deformation tensor  $\mathbf{d}$  is the symmetric part of  $\dot{\mathbf{F}} \cdot \mathbf{F}^{-1}$ .

The use of the referential gradient in the energy balance equation is justified as follows. Suppose that the deformation gradient can be expressed as the product of an elastic and a plastic deformation gradient, i.e.  $\mathbf{F} = \mathbf{F}_e \mathbf{F}_p$  (see Lee [33] and Rice [34]). The elastic deformation gradient represents the stretching of the atomic lattice along with any rigid body rotation. The plastic deformation gradient includes the flow of material through the lattice. Since heat conduction is affected primarily by the distance between atoms, a more

appropriate representation of the energy balance equation is written with  $F_c^{-T} \nabla_0$  replacing  $\nabla_0$ . However, if the magnitude of the elastic strains is small, the elastic deformation gradient is approximately a rotation. In this case, assuming that the heat conduction properties are isotropic, the form of the energy balance equation given by (2.2) is obtained when terms of order stress/elastic modulus are neglected.

The variational equation which will be used in the finite element formulation is obtained by multiplying (2.2) by  $\delta T$  and integrating over the volume in the reference configuration, and is expressed by

$$\int_A \rho c_p \frac{\partial T}{\partial t} \delta T dA = - \int_A k(\nabla_0 T) \cdot (\nabla_0 \delta T) dA + \chi \int_A \tau : d^p \delta T dA + \int_S k(\nabla_0 T \cdot \nu) \delta T dS. \quad (2.3)$$

Two dimensionless groups characterize the thermal response,

$$\xi = \frac{k}{\rho c_p \dot{\epsilon}_n h_0^2}, \quad \eta = \frac{\chi \sigma_0}{\rho c_p T_0}. \quad (2.4)$$

Here,  $\dot{\epsilon}_n$  is a reference strain rate,  $T_0$  is a reference temperature,  $h_0$  is a reference length and  $\sigma_0$  is a reference stress. The parameter  $\xi$  is the Fourier modulus, and represents the ratio of heat dissipated by conduction to internal heat storage. The quantity  $(k/\rho c_p \dot{\epsilon}_n)^{1/2}$  defines a length scale over which heat conduction effects are significant. The parameter  $\eta$  measures the magnitude of internal heat generation.

### 2.3 Boundary Conditions

We consider a block of material containing a doubly periodic array of material inhomogeneities subject to plane strain compression. As in Fig. 1, the array is imagined to be divided into square cells of dimension  $2h_0$  by  $2h_0$ , with one inhomogeneity centered in each cell. We restrict consideration to deformations such that the straight lines bounding each cell remain straight

after deformation (this is a stronger constraint than required by periodicity). Furthermore, attention is confined to deformations that preserves the mirror symmetry of the array so that straight lines connecting centers of the inhomogeneities also remain straight.

The compression axis is taken to be aligned with the  $x^2$  direction, so that the boundary conditions for the quadrant analyzed are

$$\dot{u}^1 = 0 \quad \dot{T}^2 = 0 \quad \text{at } x^1 = 0 \quad (2.5a)$$

$$\dot{u}^2 = 0 \quad \dot{T}^1 = 0 \quad \text{at } x^2 = 0 \quad (2.5b)$$

$$\dot{u}^2 = -\dot{\epsilon}_n (h_0 - U) \quad \dot{T}^1 = 0 \quad \text{at } x^2 = h_0 \quad (2.5c)$$

$$\int_0^{h_0} \dot{T}^2 dx^2 = 0 \quad \dot{u}^1 = \dot{w} \quad \text{at } x^1 = h_0 \quad (2.5d)$$

$$\nabla_0 T \cdot \nu = 0 \quad \text{on } S \quad (2.5e)$$

where  $U$  is the displacement along  $x^2 = h_0$ , defined to be positive for compression, and  $\dot{\epsilon}_n$  is the imposed nominal strain rate. The velocity of material points along  $x^1 = h_0$ , denoted by  $\dot{w}$ , is a quantity determined in the analysis as described in Section 4.2.

The boundary condition (2.5e) requires that there be no heat flux across the boundary of the quadrant analyzed. Thus, the thermal boundary condition is an overall adiabatic one, in that while there is a heat flux within a cell, there is no heat flux between cells. This gives periodicity of the temperature field with respect to the inclusion distribution.

### 3. CONSTITUTIVE RELATIONS

The flow potential surfaces are taken to be concentric cylinders centered about a stress state  $\alpha$  in stress space. The radius of the flow potential surface is denoted by  $\sigma_F$  and is given by

$$\sigma_F = \left[ \frac{3}{2} \bar{S} : \bar{S} \right]^{1/2} \quad (3.1)$$

where  $\bar{S} = S - \alpha$ . The tensor  $S$  is the Kirchhoff stress deviator, given by  $S = \tau - 1/3 \tau : I$ , where  $I$  is the identity tensor. Here, the kinematic and isotropic hardening plastic flow rules are based on Kirchhoff stress rather than on Cauchy stress. As long as elastic strains remain small, there is little difference between the two formulations.

The rate of deformation tensor is expressed as the sum of elastic and plastic parts by

$$d = d^c + d^p \quad (3.2)$$

The elastic part is given by

$$d^c = L^{-1} : \dot{\hat{T}} \quad (3.3)$$

where  $\dot{\hat{T}}$  is the Jaumann rate of Kirchhoff stress and  $L$  is a fourth order tensor representing the elastic stiffness of the material. The plastic part of the rate of deformation tensor is given by

$$d^p = \frac{3\dot{\bar{\epsilon}}}{2\sigma_F} \bar{S} \quad (3.4)$$

Here,  $\dot{\bar{\epsilon}}$  is specified by the power law relation

$$\dot{\bar{\epsilon}} = \epsilon_0 \left[ \frac{\sigma_F}{[1-\beta(T-T_0)] h(\bar{\epsilon})} \right]^{1/m} \quad (3.5)$$

where  $\epsilon_0$  is a reference strain rate,  $T_0$  is a reference temperature,  $m$  is the strain rate hardening exponent, and  $\beta$  specifies the thermal softening

characteristics of the material. This assumed linear temperature dependence is representative of carbon steels in the range 0 - 500°C, e.g. Staker [35], although at elevated temperatures the flow stress is generally a non-linear function of temperature.

We employ combined isotropic and kinematic hardening, Goel and Malvern [36], with  $h(\bar{\epsilon})$  and the evolution equation for  $\alpha$  given by

$$h(\bar{\epsilon}) = \lambda \sigma_0 [1 + \bar{\epsilon}/\epsilon_0]^N + (1-\lambda) \sigma_0 \quad (3.6)$$

$$\dot{\alpha} = \frac{2}{3} (1 - \lambda) b \dot{d}^p \quad (3.7)$$

where

$$b = \left[ \frac{\dot{\epsilon}}{\dot{\epsilon}_0} \right]^m [1 - \beta(T-T_0)]^N \frac{\sigma_0}{\epsilon_0} [1 + \bar{\epsilon}/\epsilon_0]^{N-1}. \quad (3.8)$$

Here,  $\sigma_0$  is a reference stress,  $\epsilon_0$  is a reference strain,  $N$  is the strain hardening exponent and  $\lambda$  is a constant ranging between zero and unity. Purely isotropic hardening corresponds to  $\lambda = 1$ , while purely kinematic hardening is given by  $\lambda = 0$ . The parameter  $b$ , given by (3.8), is taken so that at constant strain rate and temperature, the response for proportional loading is independent of whether the change in flow potential surface is described by isotropic hardening or by kinematic hardening, see Needleman and Tvergaard [37].

An expression for the Jaumann rate of Kirchhoff stress is obtained in terms of rate quantities by combining (3.2) through (3.4),

$$\dot{\mathbf{T}} = \mathbf{L} : \mathbf{d} - \frac{3 \dot{\bar{\epsilon}}}{2 \sigma_F} \mathbf{L} : \bar{\mathbf{S}}. \quad (3.9)$$

Although there is no explicit yielding in this formulation, for small  $m$  there is an effective yield point in that plastic strain rates are very small when the numerator is less than the denominator in (3.5).

#### 4. FINITE ELEMENT IMPLEMENTATION

##### 4.1 Rate Tangent Modulus

Using the expression for the Jaumann rate of Kirchhoff stress given by (3.9) in the incremental principle of virtual work (2.1) gives an explicit Euler time integration method. This approach requires very small time steps for numerical stability. In order to increase the stable stepsize, Peirce et al. [38] employ a formulation which results in a tangent modulus type method for solving the governing rate equations. The method is explicit in that no iterations are required. In this method the effective uniaxial plastic strain rate  $\dot{\bar{\epsilon}}$  within an increment is expressed as a linear combination of its rates at times  $t$  and  $t + \Delta t$  by

$$\dot{\bar{\epsilon}} = (1 - \theta)\dot{\bar{\epsilon}}_t + \theta\dot{\bar{\epsilon}}_{t+\Delta t} \quad (4.1)$$

where  $\theta$  is a parameter ranging from zero to unity. The plastic strain rate at time  $t + \Delta t$  is approximated by

$$\dot{\bar{\epsilon}}_{t+\Delta t} = \dot{\bar{\epsilon}}_t + \left[ \frac{\partial \dot{\bar{\epsilon}}}{\partial \sigma_F} \Big|_t \dot{\sigma}_F + \frac{\partial \dot{\bar{\epsilon}}}{\partial \bar{\epsilon}} \Big|_t \dot{\bar{\epsilon}} + \frac{\partial \dot{\bar{\epsilon}}}{\partial T} \Big|_t \dot{T} \right] \Delta t \quad (4.2)$$

An expression for  $\dot{\sigma}_F$  is obtained by differentiating (3.1) and using (3.7) and (3.9),

$$\dot{\sigma}_F = \frac{3}{2\sigma_F} \mathbf{L} : \bar{\mathbf{S}} : \mathbf{d} - [3G + (1 - \lambda)b]\dot{\bar{\epsilon}} \quad (4.3)$$

where  $G$  is the elastic shear modulus and  $b$  is given by (3.8).

Combining (4.1) through (4.3) and solving for  $\dot{\bar{\epsilon}}$  yields

$$\dot{\bar{\epsilon}} = \dot{p} + \frac{3\dot{q}}{2\sigma_F} \mathbf{L} : \bar{\mathbf{S}} : \mathbf{d} \quad (4.4)$$



where

$$\dot{p} = \frac{\dot{\bar{\epsilon}}_t}{D} \left[ 1 + \frac{\theta \beta \Delta t}{m[1 - \beta (T - T_0)]} \dot{T} \right] \quad (4.5)$$

$$\dot{q} = \frac{\theta \Delta t \dot{\bar{\epsilon}}_t}{D m \sigma_F} \quad (4.6)$$

$$D = 1 + \frac{\theta \Delta t \dot{\bar{\epsilon}}_t}{m} \left[ \frac{3G + (1 - \lambda)b}{\sigma_F} + \frac{\lambda}{h} N \frac{\sigma_0}{\epsilon_0} (1 + \bar{\epsilon}/\epsilon_0)^{N-1} \right]. \quad (4.7)$$

Substitution of (4.4) into the expression for the Jaumann rate of Kirchhoff stress given by (3.9) results in

$$\hat{\mathbf{T}} = \mathbf{C} : \mathbf{d} - \frac{3\dot{p}}{2\sigma_F} \mathbf{L} : \bar{\mathbf{S}} \quad (4.8)$$

where

$$\mathbf{C} = \mathbf{L} - \left[ \frac{3}{2\sigma_F} \right]^2 \dot{q} (\mathbf{L} : \bar{\mathbf{S}}) (\mathbf{L} : \bar{\mathbf{S}}) \quad (4.9)$$

The expression for  $\hat{\mathbf{T}}$  given by (4.8) may be used to compute the stress rates  $\dot{n}^{ij}$  needed in the incremental principle of virtual work (2.1). The details of this computation are given by Needleman [39].

#### 4.2 Enforcement of the Periodic Boundary Conditions

The mixed finite element - Rayleigh-Ritz method developed by Tvergaard [40] is used to enforce boundary condition (2.5d). Applying this method, the finite element solution of the momentum balance equation is decomposed into four sub-problems, which are chosen to insure that the boundary conditions are satisfied. The finite element discretization of the incremental principle of virtual work (2.1) is expressed as

$$K_{ij} \dot{U}_j \delta \dot{U}_i = (c_i + s_i) \delta \dot{U}_i, \quad (4.10)$$

where  $K$  is the tangent stiffness matrix,  $c$  is the right hand side which arises from the equilibrium correction term in (2.1), and  $s$  is the right hand side generated by the second term on the right side of the expression for  $\dot{A}$  given by (4.8).

The nodal velocities are expressed as a linear combination of the four sub-problems,

$$\dot{U}_i = \sum_{m=1}^4 \alpha_m \dot{U}_i^{(m)} \quad (4.11)$$

where  $\alpha_m$  are the coefficients to be determined, and the velocities  $\dot{U}^{(m)}$  are the solutions to

$$K_{ij} \dot{U}_j^{(m)} = F_i^{(m)} \quad (4.12)$$

where  $F^{(m)}$  is the right hand side for the  $m$ -th sub-problem. The vectors  $U^{(1)}$  and  $U^{(2)}$  are taken to be the velocities which arise from the equilibrium correction and the stress rate right hand sides respectively, with homogeneous boundary conditions. Therefore,  $F^{(1)} = c$  and  $F^{(2)} = s$ . In sub-problem 3 a unit horizontal velocity is prescribed at  $x^1 = h_0$ , and in sub-problem 4 a unit vertical velocity is prescribed at  $x^2 = h_0$ , with  $F^{(3)} = F^{(4)} = 0$ .

Once the velocities associated with the sub-problems have been computed, (4.11) may be substituted into (4.10) to obtain

$$\sum_{m=1}^4 R_{mn} \alpha_m = P_n \quad (4.13)$$

where

$$R_{mn} = K_{ij} \dot{U}_j^{(m)} \dot{U}_i^{(n)} \quad (4.14)$$

$$P_n = (c_i + s_i) \dot{U}_i^{(n)} \quad (4.15)$$

In order that boundary condition (2.5c) be satisfied, the coefficient  $\alpha_4$  must be the prescribed vertical velocity along  $x^2 = h_0$  (see 2.5c). Therefore, the unknown coefficients  $\alpha_i$  ( $i = 1,3$ ) are governed by

$$\sum_{m=1}^3 R_{mn} \alpha_m = P_n + \epsilon_n (h_0 - U) R_{n4} . \quad (4.16)$$

The velocity  $\dot{w}$  in (2.5d) is given by the coefficient  $\alpha_3$ .

### 4.3 Solution of the Coupled System

The differential equations resulting from the finite element discretization of the variational equations associated with the momentum and energy balance equations ((2.1) and (2.3)) are of the form

$$K_{ij}[X,U,\tau,\alpha T]_t \dot{U}_j + C_{ij}[X,U,\tau,\alpha T]_t \dot{T}_j = F_i[X,U,\tau,\alpha T]_t , \quad (4.17)$$

$$M_{ij}[X] \dot{T}_j + D_{ij}[X] T_j = Q_i[X,T,\tau,d^p] . \quad (4.18)$$

The equations may be effectively uncoupled by introducing an estimate for the nodal temperature rate at time  $t + \theta \Delta t$ , say  $\dot{T}_j^c$ , into (4.17). This is accomplished by expressing  $\dot{T}_i$  as a quadratic function of time based on its values at the previous three points in time at which the solution has been obtained, and extrapolating to obtain  $\dot{T}_i^c$ . Now the nodal velocities may be computed from the equation

$$K_{ij} \dot{U}_j = F_i - C_{ij} \dot{T}_j^c . \quad (4.19)$$

Following the solution of the nodal velocities, the displacements, stresses and internal variables are updated using a simple linear incremental updating scheme. Next, the heat generation rate  $\chi \tau : d^p$  is computed for each element, and the nodal temperatures are obtained from (4.18). The nodal temperature

rate at time  $t + \theta \Delta t$  is then calculated, and the stepsize is reduced if the computed and estimated temperature rates at that time differ by more than an allowable tolerance.

When the solution of the coupled system at time  $t + \Delta t$  has been completed, this solution becomes the new current state. The procedure is then repeated to obtain the solution for the next displacement increment.

#### 4.4 Finite Elements

The finite element meshes used in the subsequent numerical computations consist of four-node quadrilateral elements, made up of four "crossed" constant strain triangular sub-elements. In presenting results, the quadrilateral is regarded as the basic element and when reporting values of field quantities the average value over the triangles is associated with the centroid of the quadrilateral.

Nagtegaal et al. [41] have shown that an element of this type can accomodate isochoric deformations. This is of significance since the plastic strain rate is volume preserving, so that the total deformation at large strains is nearly isochoric. Another reason for using the crossed-triangle elements in the present context stems from the need to resolve localized shear bands. As discussed by Tvergaard et al. [23], a mesh composed of crossed triangles can resolve narrow shear bands in four directions - parallel with either the sides or the diagonals of the element. If the mesh is not oriented so that one of these directions coincides with the critical orientation for shear bands then localization can be significantly delayed or entirely suppressed, [23].

## 5. NUMERICAL RESULTS

### 5.1 Material Properties

The material parameters used in the calculations are chosen to be representative of a 4340 steel studied experimentally by Hartley [6]. These properties are specified by  $\sigma_0 = 1250$  MPa,  $E = 200,000$  MPa,  $\nu = 0.30$ ,  $\epsilon_0 = 0.003$ ,  $N = 0.08$ ,  $m = 0.01$ ,  $\dot{\epsilon}_0 = 0.001 \text{ sec}^{-1}$ ,  $\rho = 7833 \text{ kg/m}^3$ ,  $c_p = 465 \text{ J/kg}^\circ\text{C}$ ,  $k = 54 \text{ W/m}^\circ\text{C}$  (in the analyses involving heat conduction),  $\beta = 0.0016 \text{ per } ^\circ\text{C}$ , and  $T_0 = 20^\circ\text{C}$ . The parameter  $\chi$  in (2.2), which represents the fraction of plastic work which is locally dissipated as heat, is taken as unity in order to maximize the effects of thermal softening. Non-dimensional parameters which depend on  $\sigma_0$  are  $\sigma_0/E = 0.00625$  and  $n = 1.1714$  in (2.4). The initial undeformed state is stress free and at a uniform temperature specified by  $T_0$ .

Whether shear band development occurs under adiabatic or uniform temperature conditions strongly depends on the value of the dimensionless parameter  $\xi$  in (2.4). A priori knowledge of the thermomechanical behavior of the solid allows for the parameter  $h_0$  to be chosen so that a varied thermal response is obtained within the range of prescribed strain rates. Culver [10] calculated temperature profiles in a finite one-dimensional region for uniform heat input corresponding to a uniform strain distribution. The results show that the thermal response is essentially uniform for  $\xi > 5$ . As  $\xi$  decreases, heat conduction effects diminish, and for  $\xi < 0.02$  over one-half of the deforming region is adiabatic. For the choice of  $h_0 = 1 \text{ mm}$ , the response of the solid varies from essentially adiabatic at  $\dot{\epsilon}_n/\dot{\epsilon}_0 = 5 \times 10^5$  ( $\dot{\epsilon}_n = 500 \text{ sec}^{-1}$ ) to having a nearly uniform temperature distribution at  $\dot{\epsilon}_n/\dot{\epsilon}_0 = 5 \times 10^3$  ( $\dot{\epsilon}_n = 5 \text{ sec}^{-1}$ ).

An inhomogeneity is prescribed by specifying a value of the flow stress  $\sigma_0$  for the quadrilateral element nearest the origin equal to eighty percent of the value of the flow stress for the surrounding elements. In addition, the value of the

thermal softening parameter  $\beta$  in (3.5) for this element is taken as 0.0017 per  $^{\circ}\text{C}$  which is slightly higher than that for the other elements. Therefore, this element remains softer than the surrounding material throughout the deformation history.

## 5.2 Homogeneous Deformation

In order to provide a background for the finite element results, the behavior of the constitutive relation in homogeneous plane strain compression is analyzed. Also, the homogeneous solution is used to obtain an estimate of the critical strain at which localization will occur so that the mesh can be properly oriented for shear bands.

The homogeneous solution is obtained for an adiabatic condition. The solid is subject to the boundary conditions given by (2.5), with  $\dot{\epsilon}_n/\dot{\epsilon}_0 = 5 \times 10^5$  ( $\dot{\epsilon}_n = 500 \text{ sec}^{-1}$ ). Figs. 2 to 4 show stress-strain curves where all material properties remain constant except for one whose value is varied. All non-varying parameters are assigned the values specified previously.

Stress-strain curves are presented for various values of the strain hardening exponent  $N$  in Fig. 3. Denote the strain corresponding to the point of maximum stress by  $\epsilon_m$ . For values of  $N$  below approximately 0.20,  $\epsilon_m$  increases with increasing  $N$ . However, for values of  $N$  greater than 0.20, the trend reverses. Increasing strain hardening leads to two competing effects. Stress levels, and hence heat dissipation, are increased, which is destabilizing; on the other hand stiffness is increased.

The effects of the dimensionless parameter  $\eta$  defined in (2.4) are shown in Fig. 4. This parameter controls the magnitude of the internal heat generation rate during the deformation. Its effect on the localization strain will depend to a great

extent on the thermal softening characteristics of the material. For a given value of  $\beta$ , the strain  $\epsilon_m$  decreases rapidly as  $n$  increases.

An interesting feature of the behavior of the constitutive model in a homogeneous deformation occurs when the material softens thermally, i.e. when  $\beta$  is non-zero. When  $\beta = 0$ , the stress-strain response is independent of  $\lambda$ , the mixed hardening parameter in (3.6) and (3.7). However, the response of the solid is not independent of  $\lambda$  if it softens thermally. When  $\beta$  is positive, different stress-strain curves result for different values of  $\lambda$ , with stresses always highest in the case of kinematic hardening ( $\lambda = 0$ ). This difference is caused by the temperature dependence of the parameter  $b$  given by (3.8), which is chosen so that the isotropic hardening and kinematic hardening characterizations give identical responses in proportional loading at constant strain rate and temperature.

### 5.3 Adiabatic Analysis with Isotropic Hardening

In this calculation the response of an isotropically hardening solid under adiabatic conditions is determined. Therefore,  $\xi = 0$  in (2.4) and  $\lambda = 1$  in (3.6) and (3.7). The solid is deformed at  $\dot{\epsilon}_n/\dot{\epsilon}_0 = 5 \times 10^5$ .

The finite element mesh is composed of 20 rows of 29 quadrilateral elements, providing a total of 580 quadrilateral elements. Displaced shapes of the finite element mesh are shown in Fig. 5 at various levels of the normalized compression,  $U/h_0$ , where  $U$  is the displacement of nodes along the line  $x^2 = h_0$ . Although each quadrilateral element is comprised of four constant strain triangles, only the boundary of the deformed quadrilaterals is shown in plots of this type. The overall pattern of deformation at  $U/h_0 = 0.12$ , which is slightly before the maximum load, is essentially uniform, as shown in Fig. 5(a) at this deformation level. Only a slight non-uniformity in the deformation occurs near the inclusion. Beyond this point thermal softening dominates over strain hardening. At

$U/h_0 = 0.16$  sufficient strain accumulations have occurred so that a shear band becomes discernable in the corresponding deformed mesh plot in Fig. 5(b). As the deformation proceeds the shearing of the elements in the band occurs rapidly. Beyond  $U/h_0 = 0.18$  the shear band is fully developed, and is shown at  $U/h_0 = 0.20$  in Fig. 5(c). The shearing deformation is so intense in some of the quadrilateral elements that they have almost degenerated into triangles.

Plots of load vs. normalized compression are shown in Fig. 6. The force per unit reference area is

$$P = \frac{1}{h_0} \int_0^{h_0} T^2(h_0, x^1) dx^1. \quad (5.3)$$

The curve labelled I in Fig. 6 corresponds to this analysis. The load has been normalized with respect to the reference stress  $\sigma_0$  in this figure. The maximum value of  $P$  occurs at approximately  $U/h_0 = 0.14$ , and a shear band forms shortly thereafter. As the deformation proceeds, the rapid softening occurring in the shear band results in the continual decrease of the load.

A more quantitative description of the deformation pattern is shown by the contours of constant maximum principle logarithmic strain,  $\epsilon$ , in Fig. 7. The plots in this figure correspond to the same normalized compression levels for which the deformed meshes were presented. At  $U/h_0 = 0.12$  in Fig. 7(a) strains vary between 0.12 and 0.14 throughout most of the domain, with strains as high as 0.22 occurring at the junction of the inclusion and the surrounding material. The pattern of straining changes considerably after the attainment of the maximum load, as observed in Fig. 7(b) at  $U/h_0 = 0.16$ . Here the strain in the band is approximately twice that in the material on either side of it, which has continued to deform in a nearly uniform manner. Also evident in this figure is a section of a shear band extending through the material near the upper right section of the



mesh. This is part of a shear band which propagates from the inclusion initially located at  $(0, 2h_0)$ . Part of the shear band propagating from the inclusion initially located at  $(2h_0, 2h_0)$  also passes through the mesh in Fig. 7(b), oriented in a direction opposite to the predominant band. The strain in this band is only slightly higher than in the surrounding material, providing an indication as to the total distance of propagation of a shear band originating from any inclusion. Beyond this level of compression, any further increment of imposed deformation produces a large increase in strain within the band relative to the surrounding material, as evident in Fig. 7(c) at  $U/h_0 = 0.20$ .

The width of the shear band is essentially constant throughout the deformation. The discretization of the mesh sets a minimum width for the shear band, which is the element size. In this analysis, the shear band forms over two adjacent rows of quadrilateral elements, with the most intense deformation occurring in essentially one triangular sub-element in each of the quadrilaterals in the band.

The contours of constant temperature (in  $^{\circ}\text{C}$  and at the same deformation levels as before) in Fig. 8 illustrate the rapid localized heating that occurs. The temperatures computed in this adiabatic analysis represent only an upper bound on the true temperature distribution. Prior to the attainment of the load maximum, temperatures range between 70 and  $110^{\circ}\text{C}$  as shown in Fig. 8(a) at  $U/h_0 = 0.12$ . However, at  $U/h_0 = 0.16$ , the temperature in the band has increased to approximately  $200^{\circ}\text{C}$  while the temperature of the surrounding material has risen to about  $100^{\circ}\text{C}$ . By the time the material is compressed to 80 percent of its original height, a maximum band temperature of over  $350^{\circ}\text{C}$  has occurred, with only a small accompanying temperature rise on either side of the band.

#### 5.4 Heat Conduction with Isotropic Hardening

The effects of heat conduction on the localization process are examined in this finite element calculation. The material properties and the imposed strain rate retain the same values used in the previous analysis, with the exception of  $\xi = 2.965 \times 10^{-2}$  in (2.4). This value of  $\xi$  will be used in all subsequent calculations. The 20 by 29 finite element mesh used in the adiabatic analysis will also be used here.

This analysis shows that heat conduction causes a significant delay in the initiation of shear band localization at  $\dot{\epsilon}_n / \dot{\epsilon}_0 = 5 \times 10^5$  ( $\dot{\epsilon}_n = 500 \text{ sec}^{-1}$ ). The true stress of the elements in the shear bands does not attain a maximum value until  $U/h_0 = 0.12$ , as compared with  $U/h_0 = 0.08$  in the adiabatic case. A shear band did not become visible in a deformed mesh plot in the adiabatic analysis until  $U/h_0 = 0.16$ . In the heat conducting solid a shear band is not discernable until approximately  $U/h_0 = 0.20$ .

Deformed finite element meshes are shown in Fig. 9. Shear bands in the early stages of formation are shown in Fig. 9(a) at  $U/h_0 = 0.22$ . The shear bands are significantly broader than the ones in the adiabatic case, even as they begin to form. At this deformation level significant shearing is occurring over nearly three rows of quadrilateral elements. Heat conducted out of the shear band emanating from the inclusion at the origin results in a stiffening within this band relative to the adiabatic case. The redistribution of strain associated with this relative stiffening activates a secondary shear band, oriented perpendicular to the primary one, as shown in Fig. 9(b) at  $U/h_0 = 0.26$ . The substantially greater thermal softening in the band in the adiabatic case does not permit the formation of a secondary band. The deformed mesh in Fig. 9(c) corresponds to  $U/h_0 = 0.30$ . The normalized width of the shear bands (relative to the thermodynamic length scale  $(k/\rho c_p \dot{\epsilon}_n)^{1/2}$ ) is

0.726 as they form and increases steadily to 1.307 at  $U/h_0 = 0.30$ . In this calculation, a normalized width of unity corresponds to approximately 172 microns, so that the predicted shear band width is about 225 microns at  $U/h_0 = 0.30$ . In the adiabatic analysis, the shear band width remained nearly constant throughout the deformation history at about 100 microns.

The maximum principle logarithmic strain rate for the elements in the shear bands in the adiabatic analysis increased monotonically following the formation of the bands. However, this is not the case in the present analysis. The rate of change of maximum principle logarithmic strain for the elements in the band emanating from the origin increases to about  $\dot{\epsilon} = 1.7 \times 10^3 \text{ sec}^{-1}$  at  $U/h_0 = 0.22$ , giving a strain rate concentration in the band of 3.4. From this point until  $U/h_0 = 0.30$  the strain rate concentration decreases, dropping to about 1.6. Beyond  $U/h_0 = 0.30$  it begins to increase again.

The normalized load for the heat conducting solid is shown by curve II in Fig. 6. The load peaks at  $U/h_0 = 0.18$  and, as in the adiabatic case, a shear band forms shortly afterwards. Beyond this point the load decreases and then increases again, varying between  $1.84 \sigma_0$  and  $1.90 \sigma_0$ .

Contours of maximum principle logarithmic strain and temperature are presented in Figs. 10 and 11, respectively. They are shown at the deformation levels corresponding to the deformed meshes in Fig. 9.

### 5.5 Kinematic Hardening

This calculation is identical to the previous one with the exception that the solid hardens kinematically ( $\lambda = 0$  in (3.6) and (3.7)).

Deformed finite element meshes are presented in Fig. 12 at compression levels of  $U/h_0 = 0.19, 0.21$ , and  $0.23$ . Figs. 12(a) and (b) show the mesh just prior to and just after the formation of the shear band. Prior to the onset of

localization, the strain and temperature distributions given by the kinematically hardening model are in close agreement with the predictions of the isotropically hardening model. The stresses in the kinematically hardening solid are about five percent greater than in the isotropically hardening one. Beyond this point, the two models give very different results. The shear band in the kinematically hardening solid develops rapidly, and is fully formed shortly after its initiation, as shown in Fig. 12(c). The primary effect of kinematic hardening is to produce shear bands at lower overall strain levels relative to the isotropically hardening model. Furthermore, the shear band is narrow and well-defined, and its width varies less with increasing heat conduction than in the isotropic hardening case.

The load for the kinematically hardening solid is shown by curve III in Fig. 6. The load in this case is consistently greater than for the isotropically hardening solid, as discussed in Section 5.2. An abrupt drop in the load occurs just after the attainment of the load maximum at  $U/h_0 = 0.19$ . In fact, the load decreases much faster than in the adiabatic case. This rapid softening of the material provides evidence that strain rates in the band are quite high.

Contours of maximum principle logarithmic strain and temperature are presented in Figs. 13 and 14, respectively, at compression levels corresponding to the deformed meshes in Fig. 12. In contrast to the isotropically hardening solid, the strain rates in the band increase monotonically throughout the deformation. The strain rates in the band in this case are approximately three times greater than in the isotropically hardening solid.

### 5.6 Analyses at Lower Strain Rates

The calculations which follow examine the response of the heat conducting solid at lower imposed strain rates, specifically  $\dot{\epsilon}_n/\dot{\epsilon}_0 = 5 \times 10^4$  ( $\dot{\epsilon}_n = 50 \text{ sec}^{-1}$ ) and  $\dot{\epsilon}_n/\dot{\epsilon}_0 = 5 \times 10^3$  ( $\dot{\epsilon}_n = 5 \text{ sec}^{-1}$ ). In these calculations, the values of  $\xi$  in (2.4)

are 0.2965 and 2.965, respectively. At each of these strain rates, the response is calculated for both isotropic and kinematic hardening. In each of the analyses, all material properties are assigned the values specified in Section 5.1.

Results for the isotropically hardening solid deformed at  $\dot{\epsilon}_n/\dot{\epsilon}_0 = 5 \times 10^4$  ( $\dot{\epsilon}_n = 50 \text{ sec}^{-1}$ ) are shown in Figs. 15 through 17. Deformed finite element meshes are presented in Fig. 15 at compression levels of  $U/h_0 = 0.31$  and  $U/h_0 = 0.40$ . The mesh consists of 20 rows and 40 columns of elements. Corresponding contour plots of  $\epsilon$  and  $T$  are shown in Figs. 16 and 17, respectively. What appears to be the beginning of a rather broad shear band is evident in Fig. 15(a) at  $U/h_0 = 0.31$ , and the strain distribution in Fig. 16(a) provides supporting evidence that localization is initiating. However, as the deformation continues and the band broadens due to heat flow, the maximum principle logarithmic strain rates throughout the band never exceed  $1.5\dot{\epsilon}_n$ . What occurs is a diffuse mode of shearing, as observed in the plot of  $\epsilon$  at  $U/h_0 = 0.40$  in Fig. 16(b). The temperatures throughout the material are increasing only slightly faster than they would in a homogeneous deformation.

Results for the kinematically hardening solid deformed at  $\dot{\epsilon}_n/\dot{\epsilon}_0 = 5 \times 10^4$  are shown in Fig. 18. The mesh used in this calculation consists of 20 rows and 35 columns of elements. The strain rate in elements which are inclined at approximately 45 degrees to the compression axis begins to increase rapidly at  $U/h_0 = 0.28$ , and a shear band becomes discernable in a deformed mesh plot at  $U/h_0 = 0.31$ . The shear band is well-developed at  $U/h_0 = 0.33$ , as shown in the deformed mesh plot at this compression level in Fig. 18(a). Corresponding contours of  $\epsilon$  and  $T$  are shown in Figs. 18(b) and (c), respectively.

When the isotropically hardening solid is deformed at  $\dot{\epsilon}_n/\dot{\epsilon}_0 = 5 \times 10^3$  ( $\dot{\epsilon}_n = 5 \text{ sec}^{-1}$ ), heat conduction effects are so predominant that at no time during the deformation does the temperature vary by more than  $0.1^\circ\text{C}$  throughout the

solid. The solid was deformed to  $U/h_0 = 0.60$ , and showed no signs of shear banding. Although the strains near the inclusion are as much as ten percent greater than in the surrounding material, the isotropically hardening solid is quite resistant to localization.

A shear band does form in the kinematically hardening solid when it is deformed at  $\dot{\epsilon}_n/\dot{\epsilon}_0 = 5 \times 10^3$ . The band begins to form at  $U/h_0 = 0.40$ , and is well-defined at  $U/h_0 = 0.44$  as shown in Fig. 19(a). The mesh in this calculation consists of 20 rows and 55 columns of quadrilaterals. The corresponding strain and temperature distributions are shown in Figs. 19(b) and (c), respectively. This calculation illustrates that a shear band can form although the temperature distribution is nearly uniform. Unlike the previous analyses which involved kinematic hardening, the shear band here is broadened by the effects of heat conduction, and extends over nearly four rows of quadrilateral elements.

The results of the last two calculations (at  $\dot{\epsilon}_n/\dot{\epsilon}_0 = 5 \times 10^3$ ) are in accord with the results of Hutchinson and Tvergaard's [42] study of shear band formation in rate independent solids deforming in plane strain. The classical elastic-plastic solid with a smooth yield surface is highly resistant to localization. The flow potential surface of the kinematically hardening solid acts as a "rounded" vertex and permits localization at physically achievable strain levels [42].

## 6. CONCLUDING REMARKS

Previous analytical and numerical studies of thermal effects on shear band development have focussed on the competition between thermal softening and material hardening in circumstances where localization does not involve a change in loading path. Such analyses apply to high rate torsion tests, Costin et al. [5], Hartley [6], Duffy et al. [43]. Indeed most, if not all, detailed experimental data on thermally induced shear localization is available from such tests. However, in this investigation we have confined attention to quasi-static deformations and analyzed a model thermomechanical problem where shear localization is accompanied by a substantial shift in stress state. Even when thermal softening is the dominant destabilizing mechanism, the multi-axial constitutive response of the material plays a major role in the flow localization process.

Within the framework we have used, there is a continuous transition from thermal softening dominated localization at high rates to plastic material property dominated localization at low rates. A strong similarity of the shear localization process under adiabatic and isothermal conditions was observed by Olsen, Azrin and Tsangarakis [44] in 4340 steel and they remarked that whatever mechanism plays a role under essentially isothermal conditions undoubtedly also contributes to instability under adiabatic conditions. They discussed void initiation and growth as the destabilizing factor under isothermal conditions. While the weakening induced by progressive micro-rupture can play an important role in triggering localization under isothermal conditions, localization can also occur under these conditions when there is no prior progressive rupture on the microscale, Chang and Asaro [17], Anand and Spitzig [18] and Larsson et al. [19].

We have used kinematic hardening to model the path dependent hardening associated with a sharply curved flow potential surface. This use of kinematic hardening is intended for loading paths that do not involve extreme deviations

from proportional loading, such as reverse yielding, and is quite distinct in focus from the use of kinematic hardening as a model for Bauschinger effects. Furthermore, for the strain levels and deformation histories encountered here, the use of the Jaumann rate in the evolution equation for  $\alpha$ , (3.7), is not at issue.

Our results show a significant dependence of the course of shear band development on the multi-axial constitutive characterization of the material. Specifically, shear band development is very sensitive to the curvature of the flow potential surface; localization occurs sooner and more abruptly in a kinematic hardening solid than in an isotropic hardening solid. The effect of flow potential surface curvature on shear band development found in our calculations is consistent with previous comparisons of the behavior of kinematic hardening and isotropic hardening solids in localization phenomena, e.g. Tvergaard [25] and Hutchinson and Tvergaard [26]. In this context, the main effect of an increase in curvature of the flow potential surface is the reduction in the material's stiffness in response to an abrupt change in loading path.

The inclusion of heat conduction into the formulation introduces a material dependent length scale so that our analysis is capable of predicting shear band thickness. We find that with heat conduction, the more sharply rounded flow potential surface, as modelled by the kinematic hardening flow rule, gives rise to narrower shear bands. For the isotropic hardening solid, with heat conduction accounted for, the shear band width greatly increases with decreasing strain rate, compare Figs. 10 and 16, as well as becoming much less intense. Another effect is seen by comparing Figs. 10 and 13. For the kinematic hardening solid, Fig. 13, deformation concentrates rather rapidly into a well defined shear band. On the other hand, for the isotropically hardening solid, the concentration of deformation is slow enough for heat conduction to induce some stiffening in the shear band. This leads to the formation of the secondary set shear bands seen in Fig. 10.



### ACKNOWLEDGEMENTS

The support of this work through ARO Grant DAAG29-85-K-0003 is gratefully acknowledged. The computations reported on here were carried out at the Brown University, Division of Engineering, Computational Mechanics Facility. The acquisition of this facility was made possible by grants from the U.S. National Science Foundation (Grant ENG78-19378), the General Electric Foundation, the Ford Motor Company and the Digital Equipment Corporation.

## REFERENCES

- [1] Zener, C. and Holloman, J.H., "Effect of Strain Rate Upon Plastic Flow of Steel," *J. Appl. Phys.*, Vol. 15, p. 22, 1944.
- [2] Rogers, H.C., "Adiabatic Shearing - A Review," *Drexel University Report*, 1974.
- [3] Wright, T.W. and Batra, R.C., "Further Results on the Initiation and Growth of Adiabatic Shear Bands at High Strain Rates," *Proc. International Conference on Mechanical and Physical Behavior of Materials under Dynamic Loading*, Paris, France, 1985.
- [4] Moss, G.L. and Pond, R.B., "Inhomogeneous Thermal Changes in Copper During Plastic Elongation," *Met. Trans.*, Vol. 6A, p. 1223, 1975.
- [5] Costin, L.S., Crisman, E.E., Hawley, R.H., and Duffy, J., "On the Localization of Plastic Flow in Mild Steel Tubes under Dynamic Torsional Loading," *Proc. Second Conference on Mechanical Properties at High Rates of Strain*, ed. J. Harding, The Institute of Physics, Bristol and London, Conf. Series No. 17, pp. 90-100, 1979.
- [6] Hartley, K.A., "Temperature Measurements During the Formation of Shear Bands at High Rates of Deformation," *Ph.D. Thesis, Brown University*, 1986.
- [7] Argon, A.S., "Stability of Plastic Deformation," Chapter 8 in The Inhomogeneity of Plastic Deformation, ASM, Metals Park, OH, 1973.
- [8] Clifton, R.J., "Adiabatic Shear Banding," Chapter 8 in Materials Response to Ultra High Loading Rates, National Materials Advisory Committee, NMAB-356, 1980.
- [9] Recht, R.F., "Catastrophic Thermoplastic Shear," *J. Appl. Mech.*, pp. 189-193, 1964.
- [10] Culver, R.S., "Thermal Instability Strain in Plastic Deformation," in Metallurgical Effects at High Strain Rates, eds. R. W. Rhode, B. M. Butcher, J. R. Holland and C. H. Karnes, Plenum Press, New York, 1973.
- [11] Backman, M.E. and Finnegan, S.A., "The Propagation of Adiabatic Shear," in Metallurgical Effects at High Strain Rates, eds. R. W. Rhode, B. M. Butcher, J. R. Holland and C. H. Karnes, Plenum Press, New York, 1973.
- [12] Merzer, A.M., "Modelling of Adiabatic Shear Band Development from Small Imperfections," *J. Mech. Phys. Solids*, Vol. 30, pp. 323-338, 1982.
- [13] Fressengeas, C. and Molinari, A., "Inertial and Thermal Effects on the Localization of Plastic Flow," *Acta Metall.*, Vol. 33, 1985.

We have considered the propagation of shear bands from an initial defect, in contrast to a material stability analysis, e.g. Hill [45], Rice [24], Hutchinson and Tvergaard [26], where localization is presumed to occur instantaneously all along a narrow band. Nevertheless, the overall behavior is well represented in terms of a material instability. For example, the computed band orientations are approximately those predicted by a material instability analysis, e.g. 45 deg. from the compression axis for  $J_2$  flow theory. Also, the critical strains at which deformation concentrates in the band are in good agreement with a material instability analysis, LeMonds and Needleman [46]. In fact, this information is used, as described by Tvergaard et al. [23], in the numerical investigations to design a finite element mesh capable of resolving concentrated deformation in a narrow band.

We also note that although localization is a prominent feature of our results, the mathematical difficulties associated with loss of ellipticity do not arise. For the rate dependent constitutive relation used in this investigation, the governing equations remain elliptic as long as stresses are small compared to the elastic stiffnesses.

- [14] Olsen, G., Mescal J.F. and Azrin, M., "Adiabatic Deformation and Strain Localization," in *Proc. Conf. on Shock Waves and High Strain Rate Phenomena*, eds. M. A. Meyers and L. E. Murr, Plenum Press, New York, 1981.
- [15] Wu, F.W. and Freund, L.B., "Deformation Trapping Due to Thermoplastic Instability in One-Dimensional Wave Propagation," *J. Mech. Phys. Solids*, Vol. 32, pp. 119-132, 1984.
- [16] Shawki, T.G., "Analysis of Shear Band Formation at High Strain Rates and the Visco-Plastic Response of Polycrystals," *Ph.D. Thesis, Brown University*, 1985.
- [17] Chang, Y.W. and Asaro, R.J., "An Experimental Study of Shear Localization in Aluminum-Copper Single Crystals," *Acta Metall.*, Vol. 29, p. 241, 1981.
- [18] Anand, L. and Spitzig, W.A., "Initiation of Localized Shear Bands in Plane Strain," *J. Mech. Phys. Solids*, Vol. 28, pp. 113-128, 1980.
- [19] Larsson, M., Needleman, A., Tvergaard, V. and Storakers, B., "Instability and Failure of Internally Pressurized Ductile Metal Cylinders," *J. Mech. Phys. Solids*, Vol. 30, pp. 121-154, 1982.
- [20] Rice, J.R., "On the Structure of Stress-Strain Relations for Time-Dependent Plastic Deformation in Metals," *J. Appl. Mech.*, Vol. 37, pp. 728-737, 1970.
- [21] Needleman, A. and Rice, J.R., "Limits to Ductility Set by Plastic Flow Localization," in *Mechanics of Sheet Metal Forming*, eds. D. P. Koistinen and N. M. Wang, Plenum Press, New York, 1978.
- [22] Asaro, R.J., "Geometrical Effects in the Inhomogeneous Deformation of Ductile Single Crystals," *Acta Metall.*, Vol. 27, pp. 445-453, 1979.
- [23] Tvergaard, V., Needleman, A. and Lo, K.K., "Flow Localization in the Plane Strain Tensile Test," *J. Mech. Phys. Solids*, Vol. 29, pp. 115-142, 1981.
- [24] Rice, J.R., "The Localization of Plastic Deformation," in *Theoretical and Applied Mechanics*, ed. W. T. Koiter, North-Holland, Amsterdam, pp. 207-220, 1976.
- [25] Tvergaard, V., "Effect of Kinematic Hardening on Localized Necking in Biaxially Stretched Sheets," *Int. J. Mech. Sci.*, Vol. 20, pp. 651-658, 1978.
- [26] Hutchinson, J.W. and Tvergaard, V., "Shear Band Formation in Plane Strain," *Int. J. Solids Struct.*, Vol. 17, pp. 451-470, 1981.
- [27] Abeyaratne, R. and Triantafyllidis, N., "The Emergence of Shear Bands in Plane Strain," *Int. J. Solids and Structures*, Vol. 17, pp. 1113-1134, 1981.

- [28] Wu, F.W., Freund, L.B. and Toullos, M., "Initiation and Propagation of Shear Bands in Antiplane Shear Deformation," *Brown University Report DAAG-29-81-K-0121*, 1984.
- [29] Needleman, A., "A Numerical Study of Necking in Circular Cylindrical Bars," *J. Mech. Phys. Solids*, Vol. 20, pp. 111-127, 1972.
- [30] Tvergaard, V., "Effect of Thickness Inhomogeneities in Internally Pressurized Spherical Shells," *J. Mech. Phys. Solids*, Vol. 24, pp. 291-304, 1976.
- [31] Peirce, D., Asaro, R.J. and Needleman, A., "Material Rate Dependence and Localized Deformation in Crystalline Solids," *Acta Metall.*, Vol. 31, No. 12, pp. 1951-1976, 1983.
- [32] Taylor, G.I. and Quinney, H., "The Latent Energy Remaining in a Metal After Cold Working," *Proc. Roy. Soc. London*, p. 143, 1934.
- [33] Lee, E.H., "Elastic-Plastic Deformation at Finite Strains," *J. Appl. Mech.*, Vol. 36, pp. 1-6, 1969.
- [34] Rice, J.R., "Inelastic Constitutive Relations for Solids: An Internal Variable Theory and its Application to Metal Plasticity," *J. Mech. Phys. Solids*, Vol. 19, pp. 433-455, 1971.
- [35] Staker, M.R., "The Relation Between Adiabatic Shear Instability Strain and Material Properties," *Acta Metall.*, Vol. 29, pp. 683-689, 1981.
- [36] Goel, R.P. and Malvern, L.E., "Biaxial Plastic Simple Waves with Combined Kinematic and Isotropic Hardening," *J. Appl. Mech.*, Vol. 37, 1970.
- [37] Needleman, A. and Tvergaard, V., "Limits to Formability in Rate-Sensitive Metal Sheets," in Mechanical Behavior of Materials - IV, ed. by J. Carlsson and N. G. Ohlson, Pergamon, 1984.
- [38] Peirce, D., Shih, C.F. and Needleman, A., "A Tangent Modulus Method for Rate Dependent Solids," *Computers and Structures*, Vol. 18, pp. 875-887, 1984.
- [39] Needleman, A., "Finite Elements for Finite Strain Plasticity Problems," in Plasticity of Metals at Finite Strain: Theory, Computation and Experiment, ed. by E. H. Lee and R. H. Mallett, pp. 387-436, Stanford University, 1982.
- [40] Tvergaard, V., "Effect of Thickness Inhomogeneities in Internally Pressurized Spherical Shells," *J. Mech. Phys. Solids*, Vol. 24, pp. 291-304, 1976.

- [41] Nagtegaal, J.C., Parks, D.M. and Rice, J.R., "On Numerically Accurate Finite Element Solutions in the Fully Plastic Range," *Comp. Meth. Appl. Mech. Engr.*, Vol. 4, pp. 153-177, 1974.
- [42] Hutchinson, J.W. and Tvergaard, V., "Shear Band Formation in Plane Strain," *Int. J. Solids Struct.*, Vol. 17, pp. 451-470, 1981.
- [43] Hartley, K.A., Duffy, J. and Hawley, R.H., "Measurement of the Temperature Profile During Shear Band Formation in Steels Deforming at High Strain Rates," Brown University Report DAAG29-85-K-0003/2, 1986.
- [44] Olson, G.B., Azrin, M. and Tsangarakis, N.J., "Plastic Shear Instability in 4340 Steel," *Proc. of the 29th Sagamore Army Conference - Materials Behavior under High Stress and Ultrahigh Loading Rates - Part II*, 1984.
- [45] Hill, R., "Acceleration Waves in Solids," *J. Mech. Phys. Solids*, Vol. 13, pp. 10-16, 1962.
- [46] LeMonds, J. and Needleman, A. "A Flow Localization Analysis Incorporating Heat Conduction Effects," to be published.

## FIGURE CAPTIONS

- Fig. 1 The undeformed periodic array of inclusions. The shaded area in this figure represents the region of the domain which is modelled numerically.
- Fig. 2 Normalized true stress vs. logarithmic strain for a homogeneous deformation in plane strain compression with  $\dot{\epsilon}_n/\dot{\epsilon}_0 = 5 \times 10^5$  ( $\dot{\epsilon}_n = 500 \text{ sec}^{-1}$ ) and various values of the thermal softening parameter  $\beta$  in (3.5). The values of all other material properties are specified in Section 5.1.
- Fig. 3 Normalized true stress vs. logarithmic strain for a homogeneous deformation in plane strain compression with  $\dot{\epsilon}_n/\dot{\epsilon}_0 = 5 \times 10^5$  ( $\dot{\epsilon}_n = 500 \text{ sec}^{-1}$ ) and various values of the strain hardening exponent  $N$  in (3.6). The values of all other material properties are specified in Section 5.1.
- Fig. 4 Normalized true stress vs. logarithmic strain for a homogeneous deformation in plane strain compression with  $\dot{\epsilon}_n/\dot{\epsilon}_0 = 5 \times 10^5$  ( $\dot{\epsilon}_n = 500 \text{ sec}^{-1}$ ) and various values of the non-dimensional parameter  $\eta$  in (2.4) which measures the magnitude of the rate of internal heat generation. The values of all other material properties are specified in Section 5.1.
- Fig. 5 Deformed finite element meshes for the case where  $\dot{\epsilon}_n/\dot{\epsilon}_0 = 5 \times 10^5$  ( $\dot{\epsilon}_n = 500 \text{ sec}^{-1}$ ), with isotropic hardening and  $\xi = 0$  in (2.4) being the adiabatic limit. The values of all other material properties are specified in Section 5.1. (a)  $U/h_0 = 0.12$ , (b)  $U/h_0 = 0.16$  and (c)  $U/h_0 = 0.20$ .

Fig. 6 Normalized load vs. displacement for the cases where (I)  $\dot{\epsilon}_n/\dot{\epsilon}_0 = 5 \times 10^5$  and  $\xi = 0$  with isotropic hardening; (II)  $\dot{\epsilon}_n/\dot{\epsilon}_0 = 5 \times 10^5$  and  $\xi = 2.965 \times 10^{-2}$  with isotropic hardening; and (III)  $\dot{\epsilon}_n/\dot{\epsilon}_0 = 5 \times 10^5$  and  $\xi = 2.965 \times 10^{-2}$  with kinematic hardening. The Fourier modulus  $\xi$  is defined in (2.4), with  $\xi = 0$  being the adiabatic limit, and the non-zero value of  $\xi$  results from the thermal conductivity  $k = 54 \text{ W/m}^\circ\text{C}$ . The values of all other material properties are specified in Section 5.1.

Fig. 7 Contours of maximum principle logarithmic strain for the case where  $\dot{\epsilon}_n/\dot{\epsilon}_0 = 5 \times 10^5$  ( $\dot{\epsilon}_n = 500 \text{ sec}^{-1}$ ), with isotropic hardening and  $\xi = 0$  in (2.4) being the adiabatic limit. The values of all other material properties are specified in Section 5.1. (a)  $U/h_0 = 0.12$ , (b)  $U/h_0 = 0.16$  and (c)  $U/h_0 = 0.20$ .

Fig. 8 Contours of temperature (in  $^\circ\text{C}$ ) for the case where  $\dot{\epsilon}_n/\dot{\epsilon}_0 = 5 \times 10^5$  ( $\dot{\epsilon}_n = 500 \text{ sec}^{-1}$ ), with isotropic hardening and  $\xi = 0$  in (2.4) being the adiabatic limit. The values of all other material properties are specified in Section 5.1. (a)  $U/h_0 = 0.12$ , (b)  $U/h_0 = 0.16$  and (c)  $U/h_0 = 0.20$ . The initial temperature is  $20^\circ\text{C}$ .

Fig. 9 Deformed finite element meshes for the case where  $\dot{\epsilon}_n/\dot{\epsilon}_0 = 5 \times 10^5$  ( $\dot{\epsilon}_n = 500 \text{ sec}^{-1}$ ), with isotropic hardening and  $\xi = 2.965 \times 10^{-2}$  in (2.4). The values of all other material properties are specified in Section 5.1. (a)  $U/h_0 = 0.22$ , (b)  $U/h_0 = 0.26$  and (c)  $U/h_0 = 0.30$ .

Fig. 10 Contours of maximum principle logarithmic strain for the case where  $\dot{\epsilon}_n/\dot{\epsilon}_0 = 5 \times 10^5$  ( $\dot{\epsilon}_n = 500 \text{ sec}^{-1}$ ), with isotropic hardening and  $\xi = 2.965 \times 10^{-2}$  in (2.4). The values of all other material properties are specified in Section 5.1. (a)  $U/h_0 = 0.22$ , (b)  $U/h_0 = 0.26$  and (c)  $U/h_0 = 0.30$ .



Fig. 11 Contours of temperature (in  $^{\circ}\text{C}$ ) for the case where  $\dot{\epsilon}_n/\dot{\epsilon}_0 = 5 \times 10^5$  ( $\dot{\epsilon}_n = 500 \text{ sec}^{-1}$ ), with isotropic hardening and  $\xi = 2.965 \times 10^{-2}$  in (2.4). The values of all other material properties are specified in Section 5.1. (a)  $U/h_0 = 0.22$ , (b)  $U/h_0 = 0.26$  and (c)  $U/h_0 = 0.30$ . The initial temperature is  $20^{\circ}\text{C}$ .

Fig. 12 Deformed finite element meshes for the case where  $\dot{\epsilon}_n/\dot{\epsilon}_0 = 5 \times 10^5$  ( $\dot{\epsilon}_n = 500 \text{ sec}^{-1}$ ), with kinematic hardening and  $\xi = 2.965 \times 10^{-2}$  in (2.4). The values of all other material properties are specified in Section 5.1. (a)  $U/h_0 = 0.19$ , (b)  $U/h_0 = 0.21$  and (c)  $U/h_0 = 0.23$ .

Fig. 13 Contours of maximum principle logarithmic strain for the case where  $\dot{\epsilon}_n/\dot{\epsilon}_0 = 5 \times 10^5$  ( $\dot{\epsilon}_n = 500 \text{ sec}^{-1}$ ), with kinematic hardening and  $\xi = 2.965 \times 10^{-2}$  in (2.4). The values of all other material properties are specified in Section 5.1. (a)  $U/h_0 = 0.19$ , (b)  $U/h_0 = 0.21$  and (c)  $U/h_0 = 0.23$ .

Fig. 14 Contours of temperature (in  $^{\circ}\text{C}$ ) for the case where  $\dot{\epsilon}_n/\dot{\epsilon}_0 = 5 \times 10^5$  ( $\dot{\epsilon}_n = 500 \text{ sec}^{-1}$ ), with kinematic hardening and  $\xi = 2.965 \times 10^{-2}$  in (2.4). The values of all other material properties are specified in Section 5.1. (a)  $U/h_0 = 0.19$ , (b)  $U/h_0 = 0.21$  and (c)  $U/h_0 = 0.23$ . The initial temperature is  $20^{\circ}\text{C}$ .

Fig. 15 Deformed finite element meshes for the case where  $\dot{\epsilon}_n/\dot{\epsilon}_0 = 5 \times 10^4$  ( $\dot{\epsilon}_n = 50 \text{ sec}^{-1}$ ), with isotropic hardening and  $\xi = 0.2965$  in (2.4). The values of all other material properties are specified in Section 5.1. (a)  $U/h_0 = 0.31$ , (b)  $U/h_0 = 0.40$ .

Fig. 16 Contours of maximum principle logarithmic strain for the case where  $\dot{\epsilon}_n/\dot{\epsilon}_0 = 5 \times 10^4$  ( $\dot{\epsilon}_n = 50 \text{ sec}^{-1}$ ), with isotropic hardening and  $\xi = 0.2965$  in (2.4). The values of all other material properties are specified in Section 5.1. (a)  $U/h_0 = 0.31$ , (b)  $U/h_0 = 0.40$ .

Fig. 17 Contours of temperature (in  $^{\circ}\text{C}$ ) for the case where  $\dot{\epsilon}_n/\dot{\epsilon}_0 = 5 \times 10^4$  ( $\dot{\epsilon}_n = 50 \text{ sec}^{-1}$ ), with isotropic hardening and  $\xi = 0.2965$  in (2.4). The values of all other material properties are specified in Section 5.1. (a)  $U/h_0 = 0.31$ ; (b)  $U/h_0 = 0.40$ . The initial temperature is  $20^{\circ}\text{C}$ .

Fig. 18 Results at  $U/h_0 = 0.33$  for the case where  $\dot{\epsilon}_n/\dot{\epsilon}_0 = 5 \times 10^4$  ( $\dot{\epsilon}_n = 50 \text{ sec}^{-1}$ ), with kinematic hardening and  $\xi = 0.2965$  in (2.4); (a) deformed finite element mesh, (b) contours of maximum principle logarithmic strain, and (c) contours of temperature (in  $^{\circ}\text{C}$ ). The initial temperature is  $20^{\circ}\text{C}$ . The values of all other material properties are specified in Section 5.1.

Fig. 19 Results at  $U/h_0 = 0.44$  for the case where  $\dot{\epsilon}_n/\dot{\epsilon}_0 = 5 \times 10^3$  ( $\dot{\epsilon}_n = 5 \text{ sec}^{-1}$ ) and  $\xi = 2.965$  in (2.4) with kinematic hardening; (a) Deformed finite element mesh, (b) contours of maximum principle logarithmic strain, and (c) contours of temperature (in  $^{\circ}\text{C}$ ). The initial temperature is  $20^{\circ}\text{C}$ . The values of all other material properties are specified in Section 5.1.

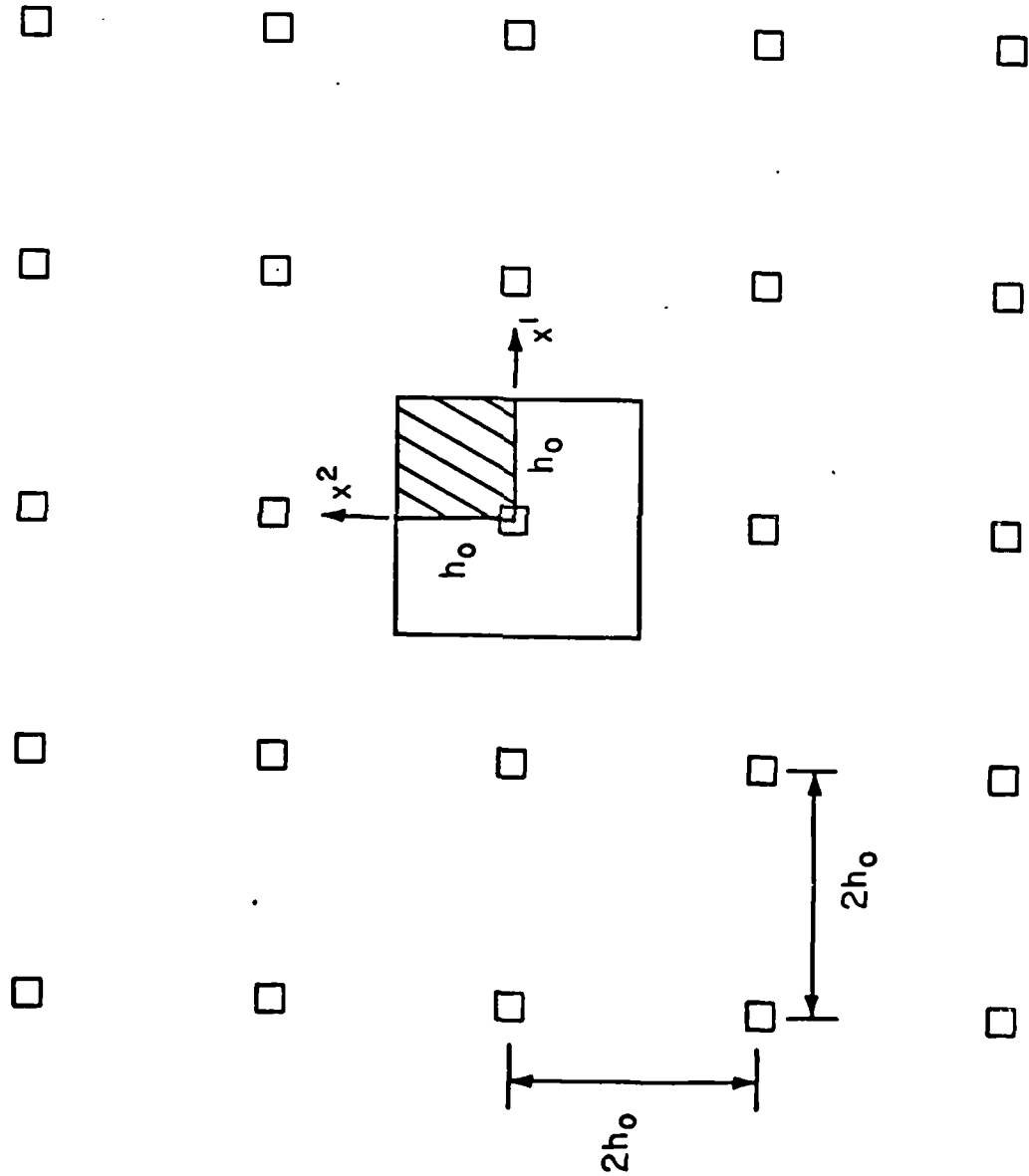


FIGURE 1

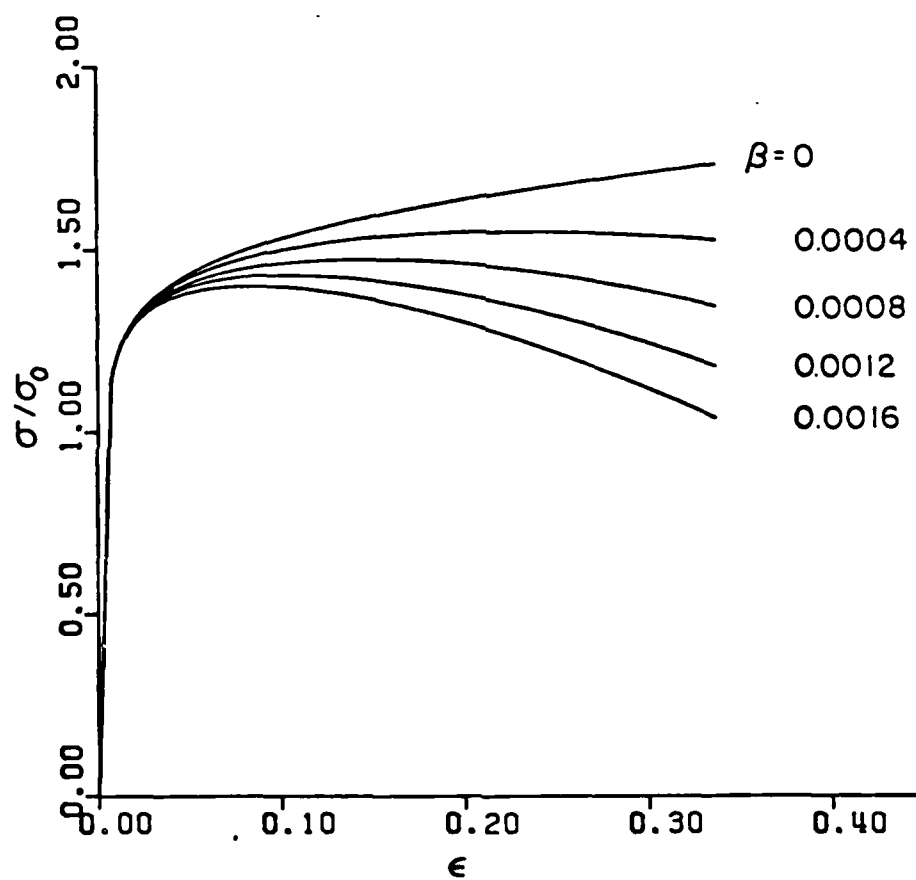


FIGURE 2

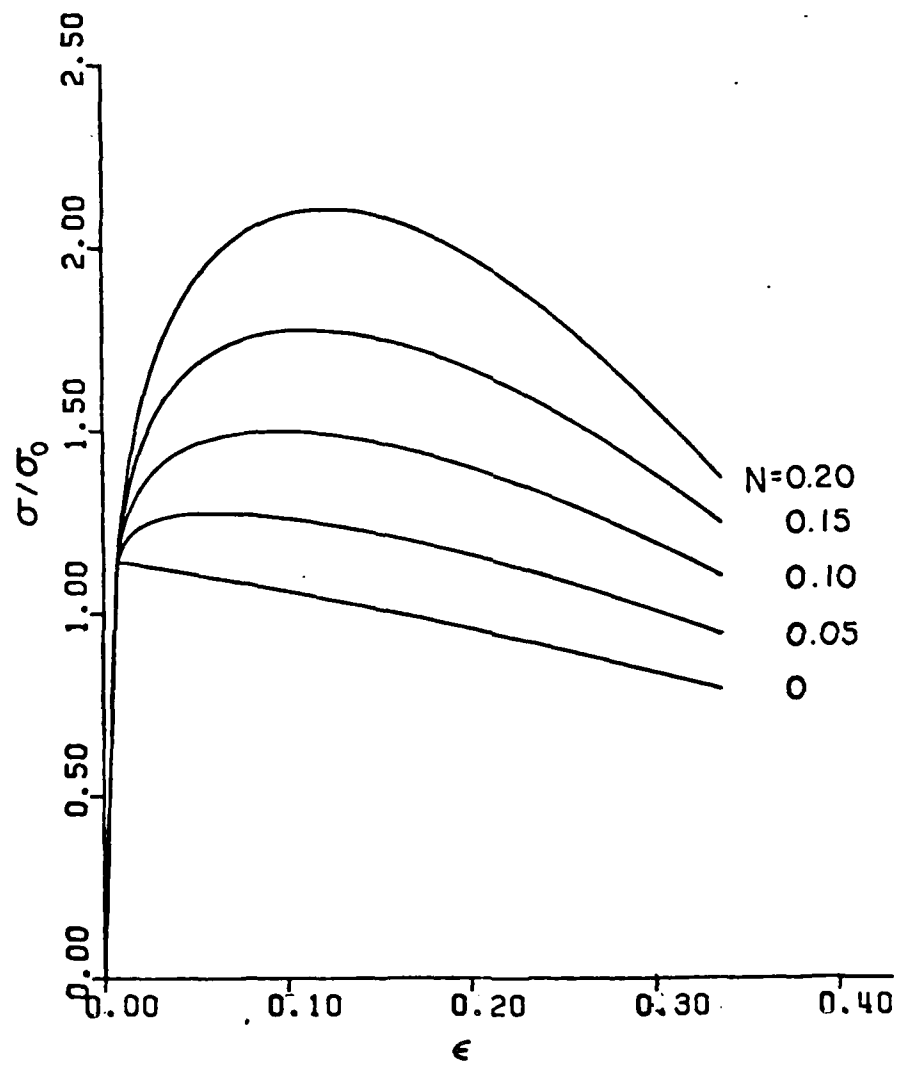


FIGURE 3

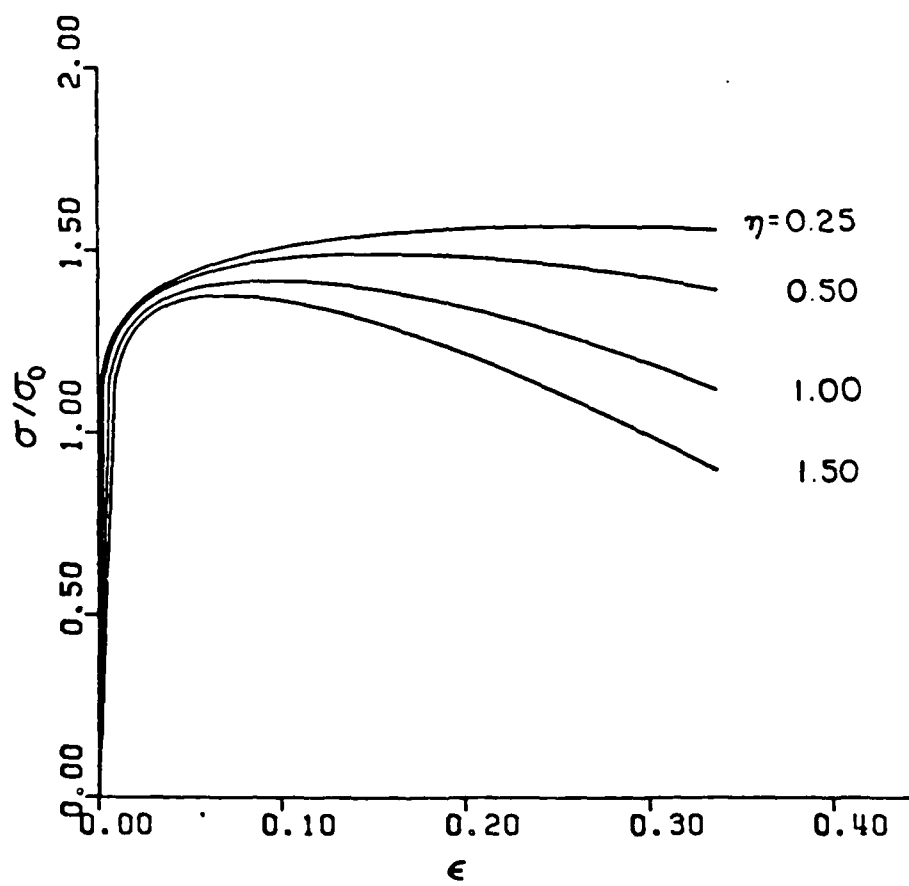
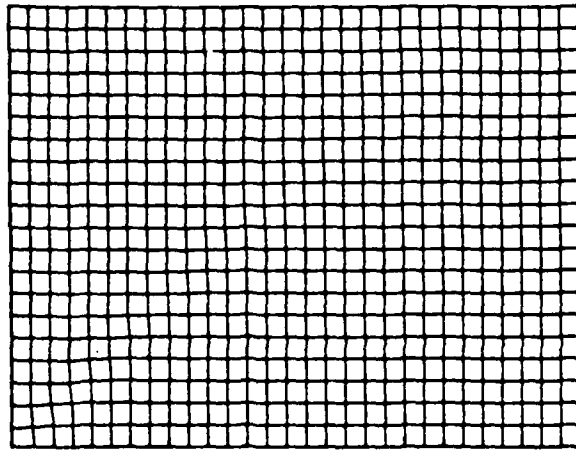
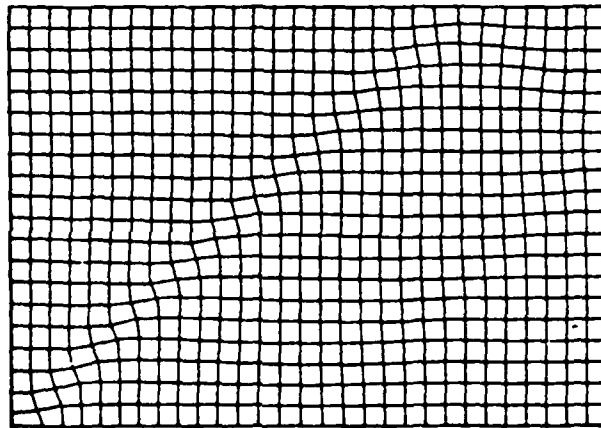


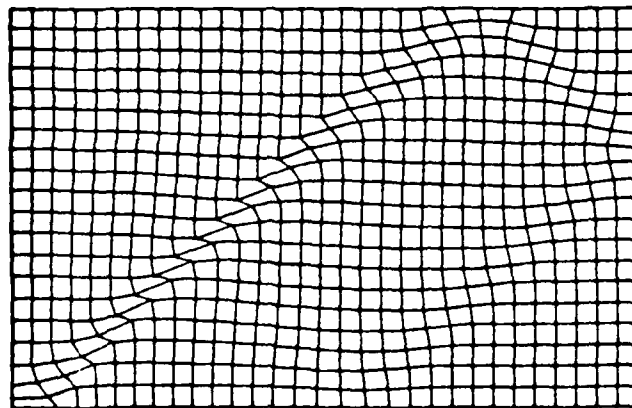
FIGURE 4



(a)



(b)



(c)

FIGURE 5

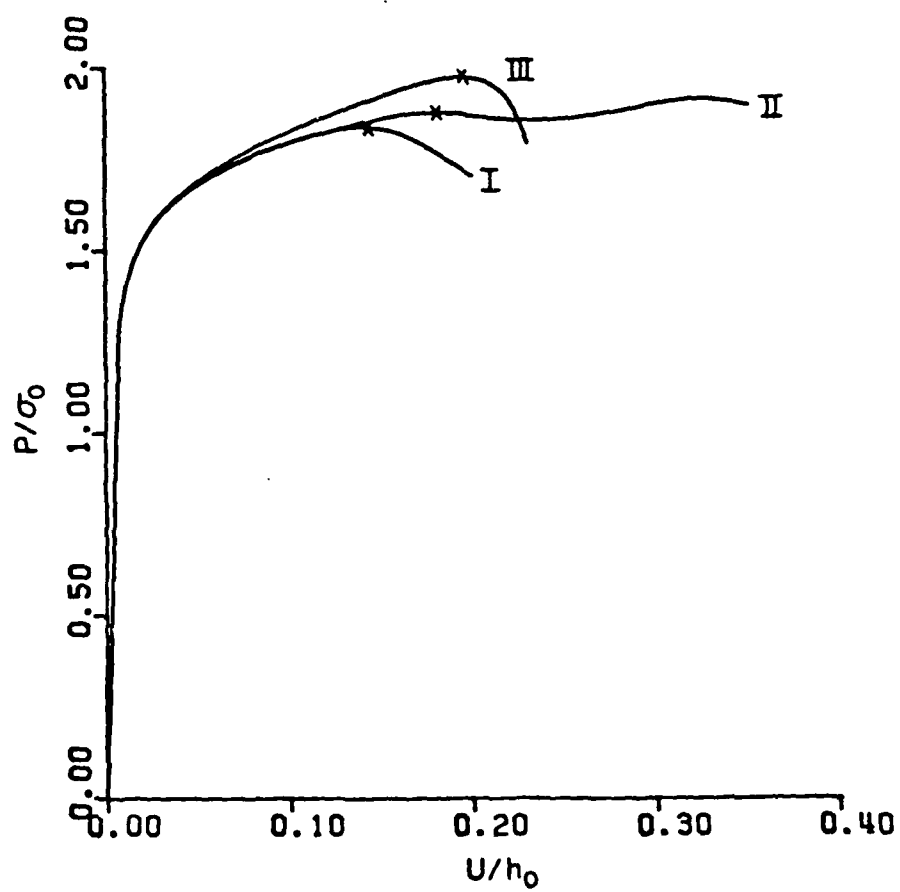
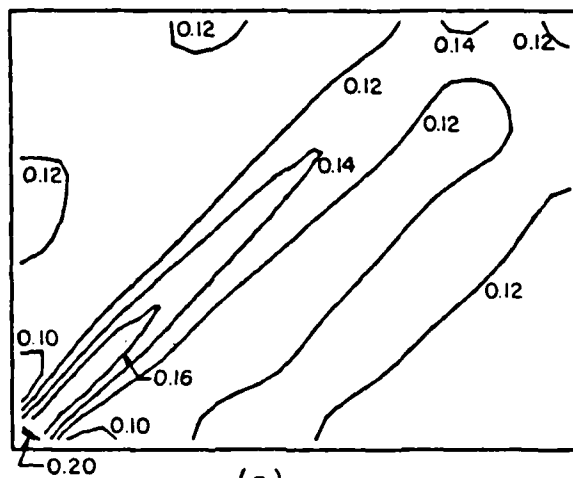
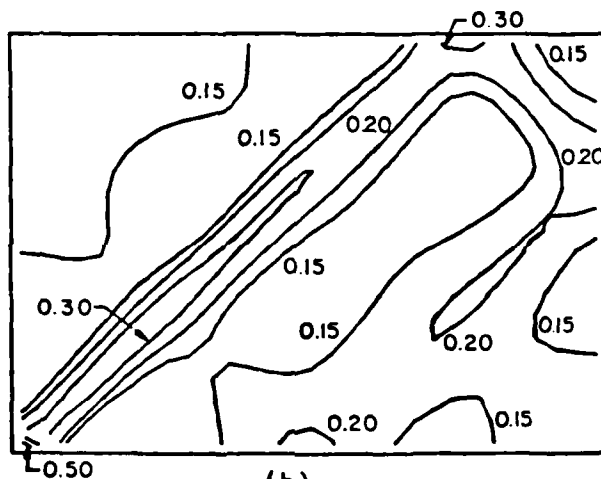


FIGURE 6

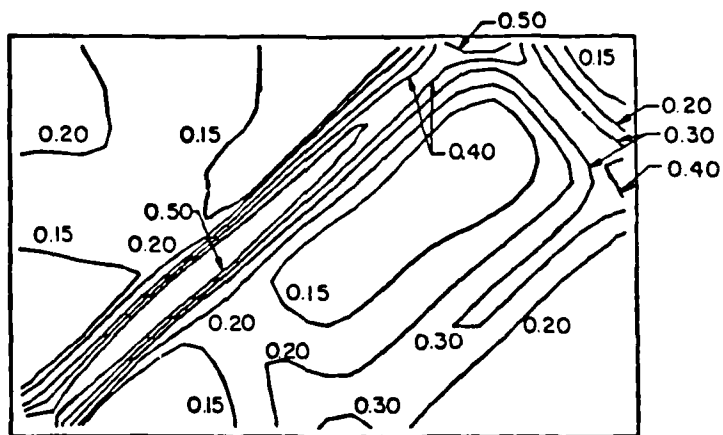




(a)

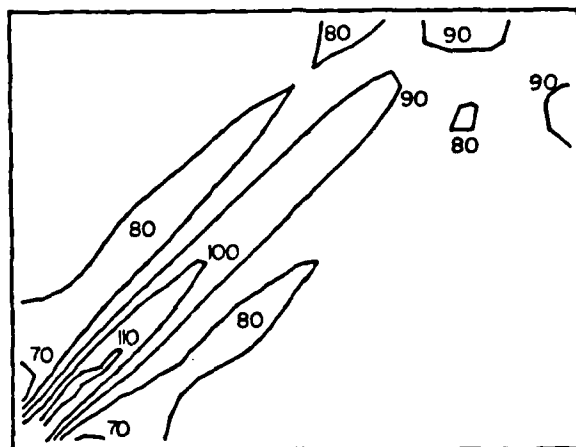


(b)

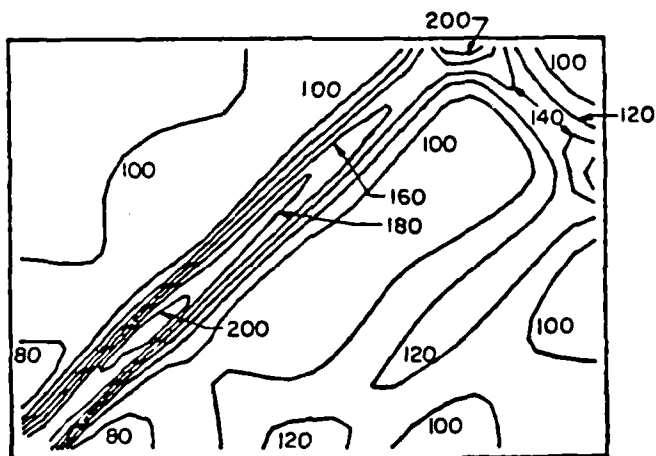


(c)

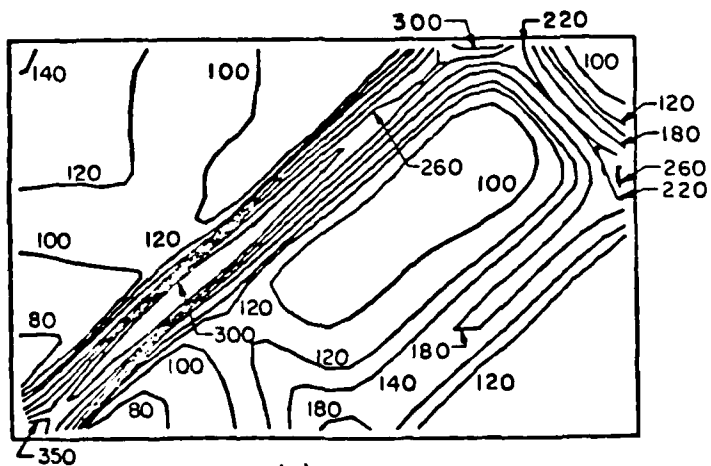
FIGURE 7



(a)

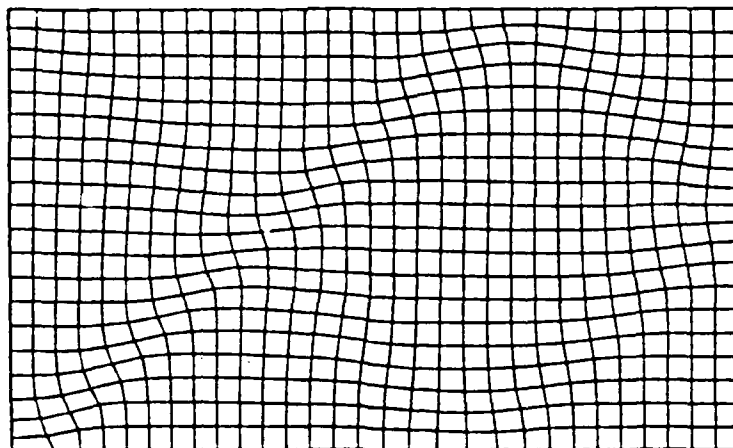


(b)

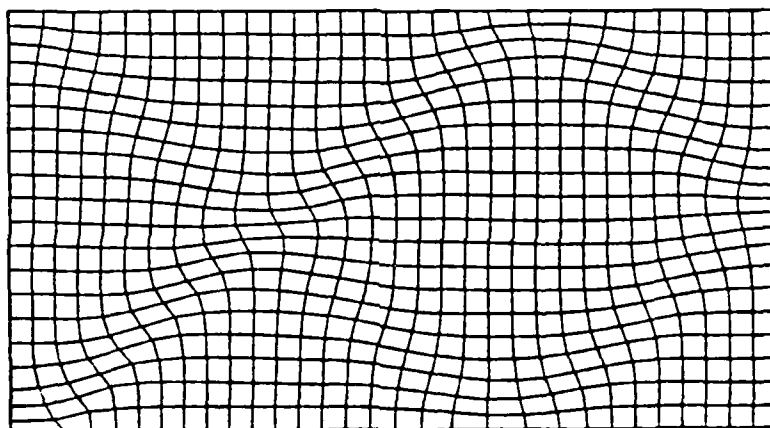


(c)

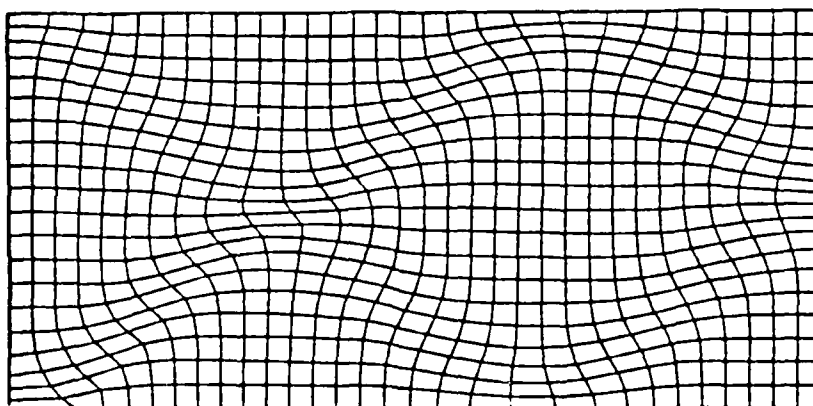
FIGURE 8



(a)

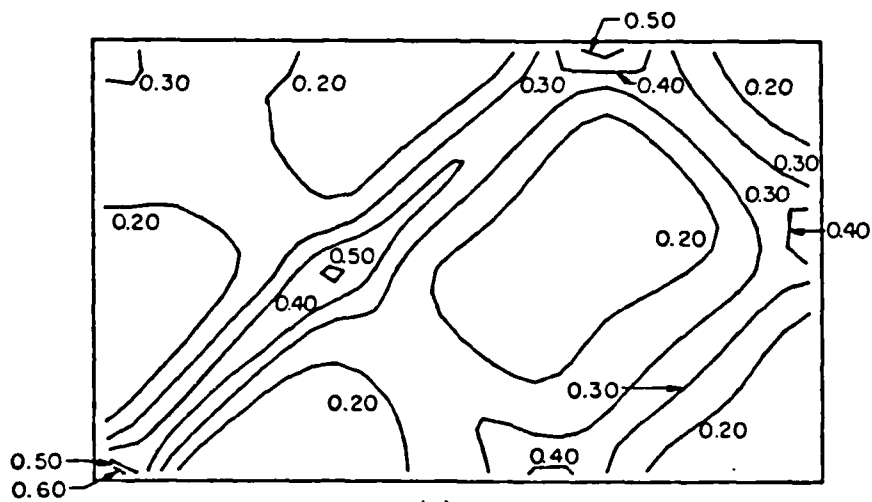


(b)

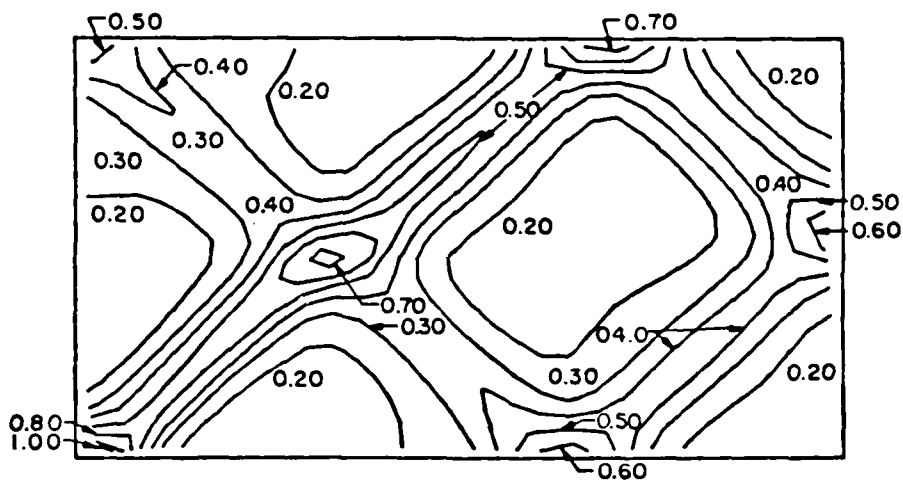


(c)

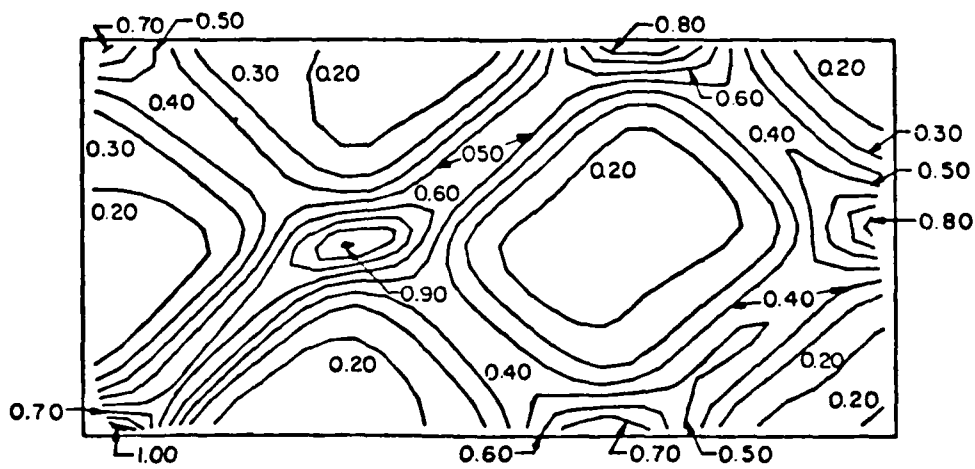
**FIGURE 9**



(a)

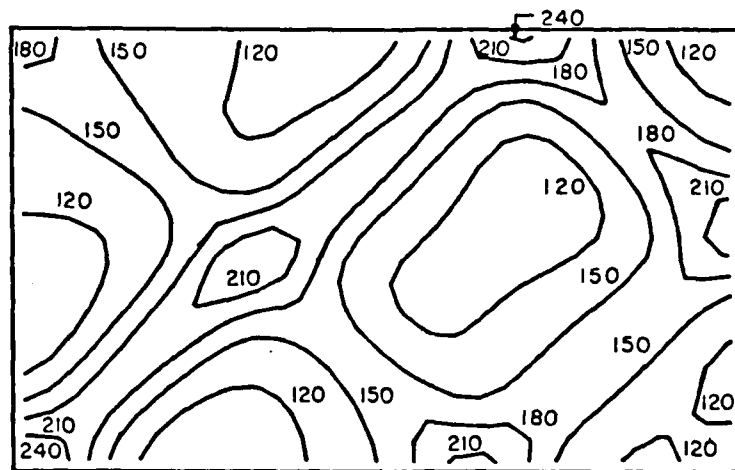


(b)

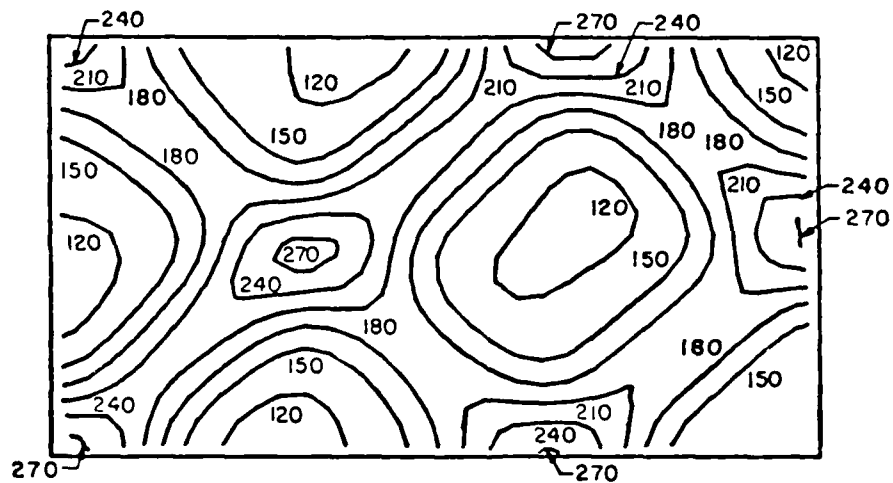


(c)

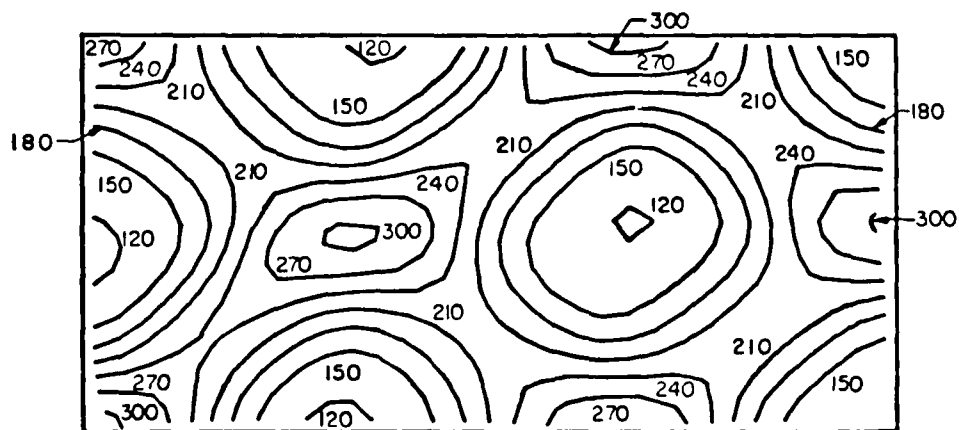
FIGURE 10



(a)

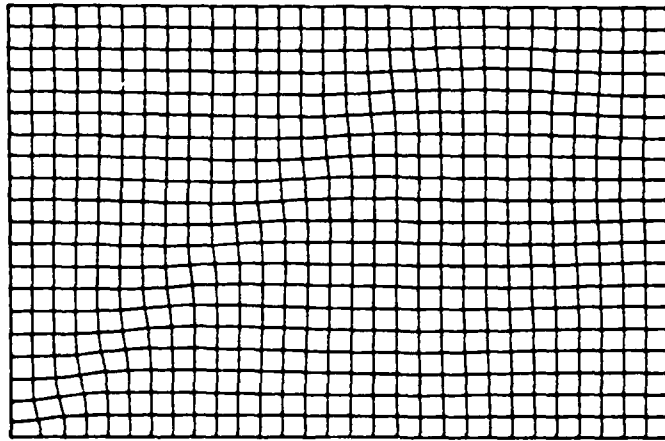


(b)

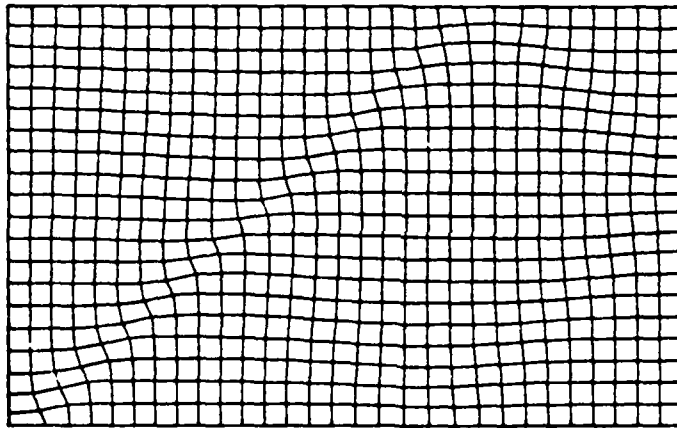


(c)

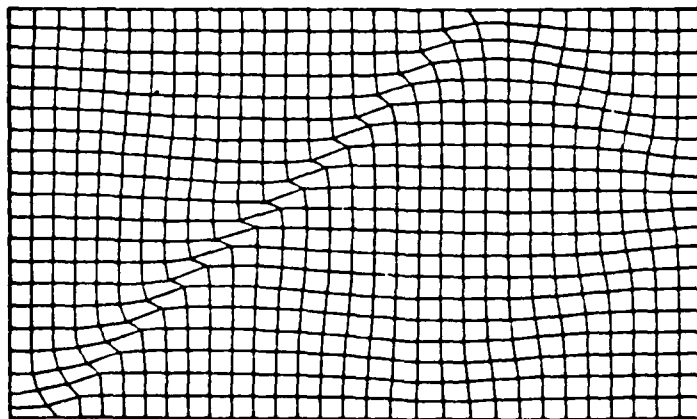
FIGURE 11



(a)

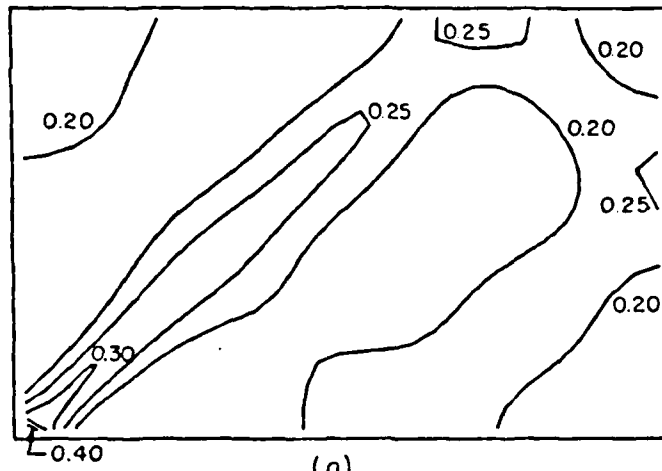


(b)

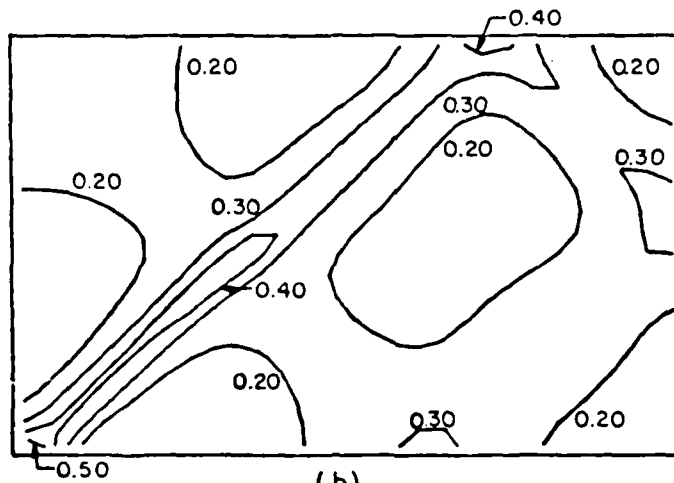


(c)

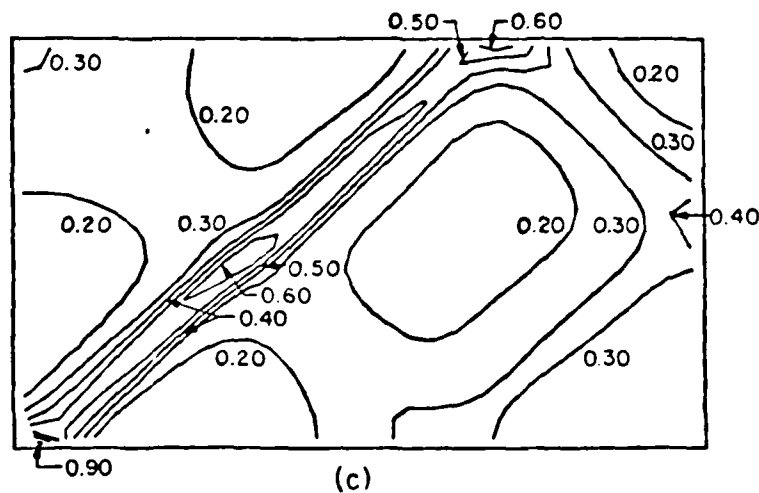
FIGURE 12



(a)

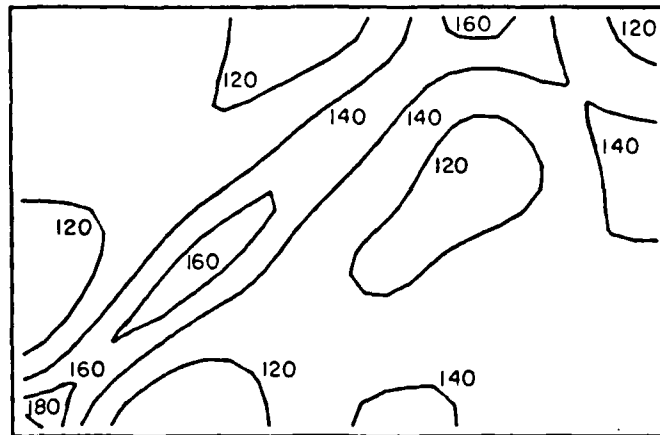


(b)

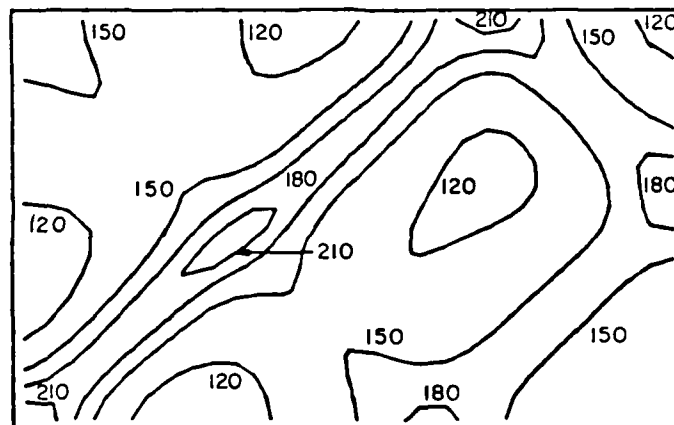


(c)

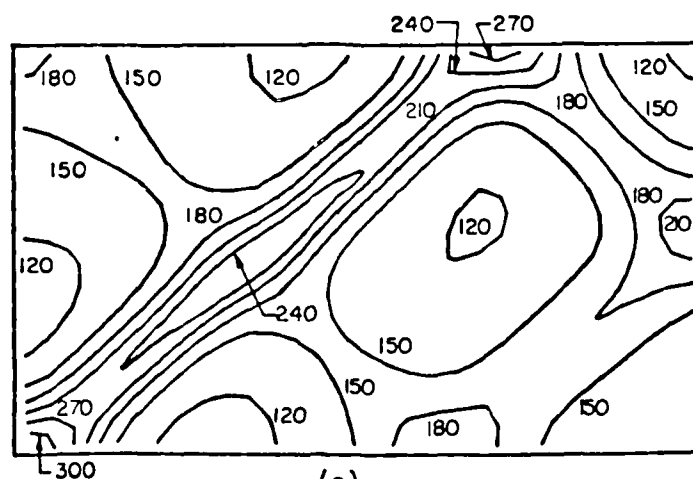
FIGURE 13



(a)



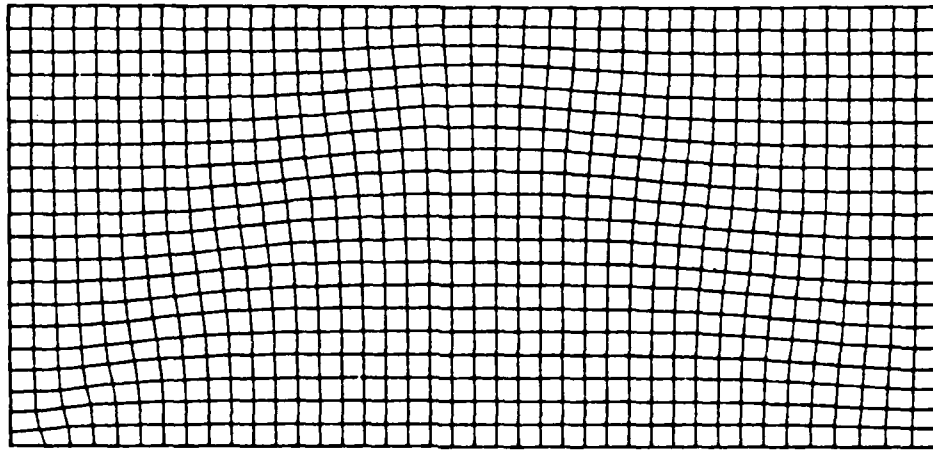
(b)



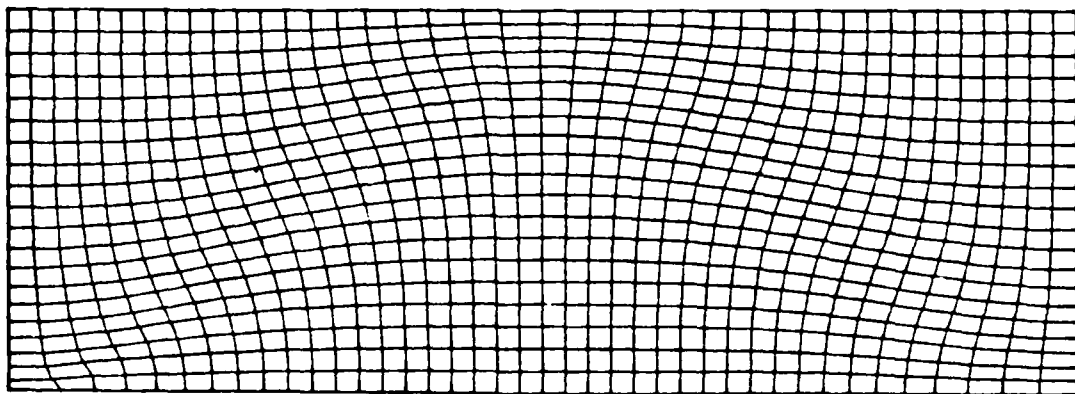
(c)

FIGURE 14





(a)



(b)

FIGURE 15

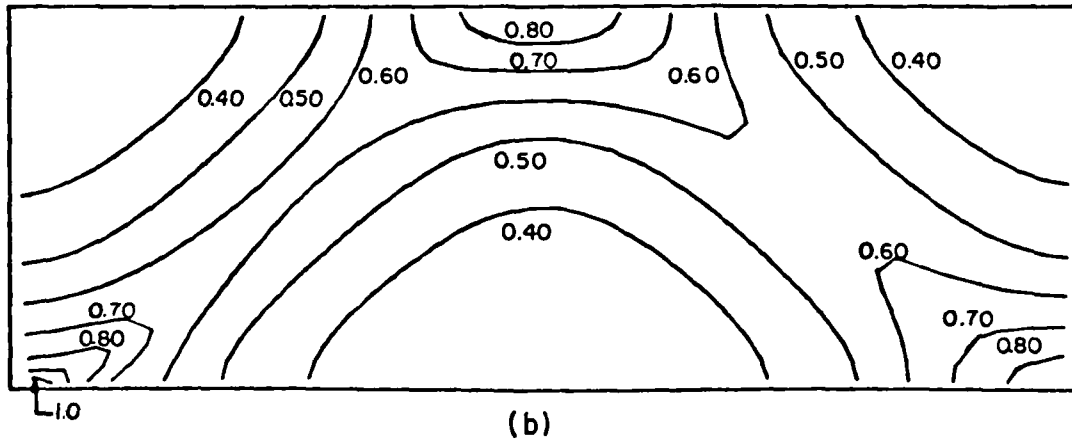
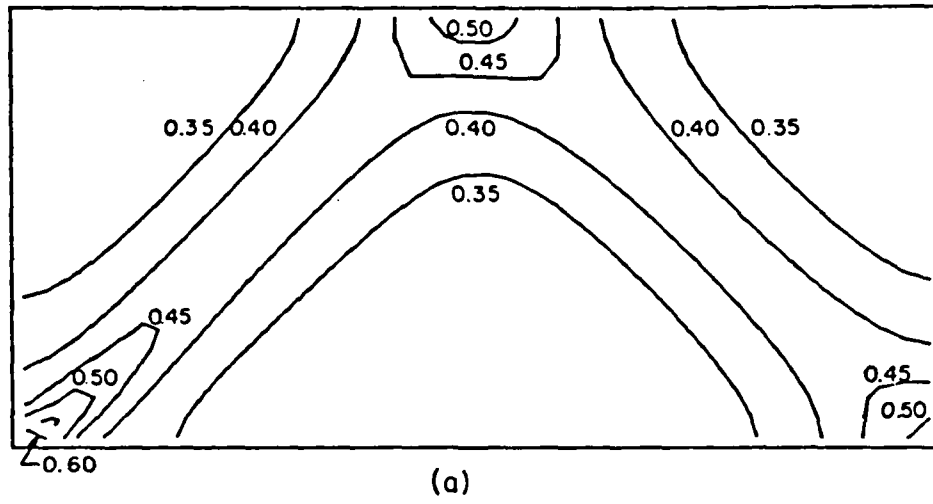
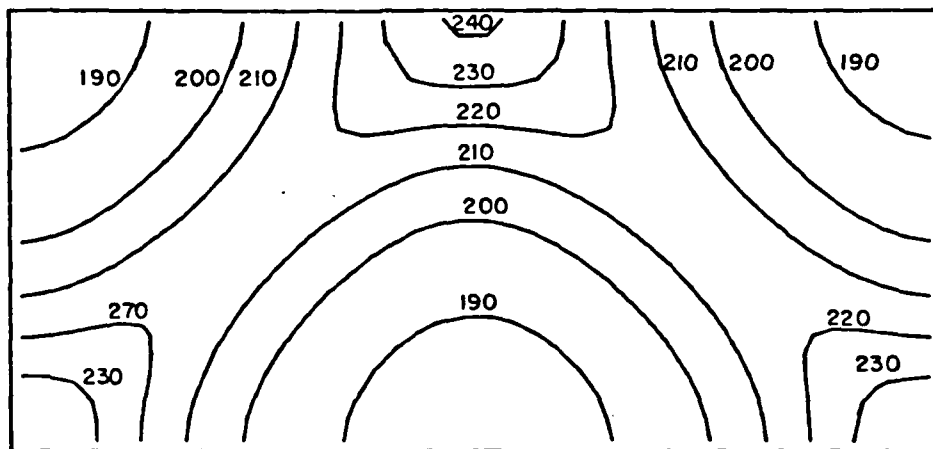
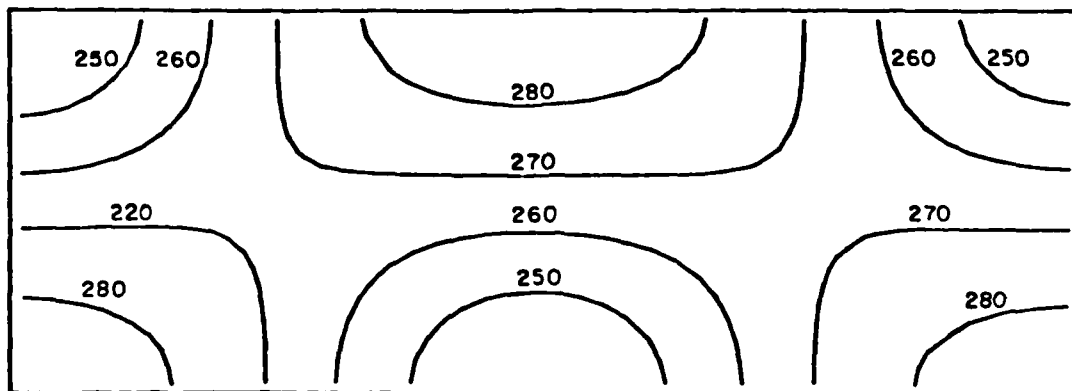


FIGURE 16

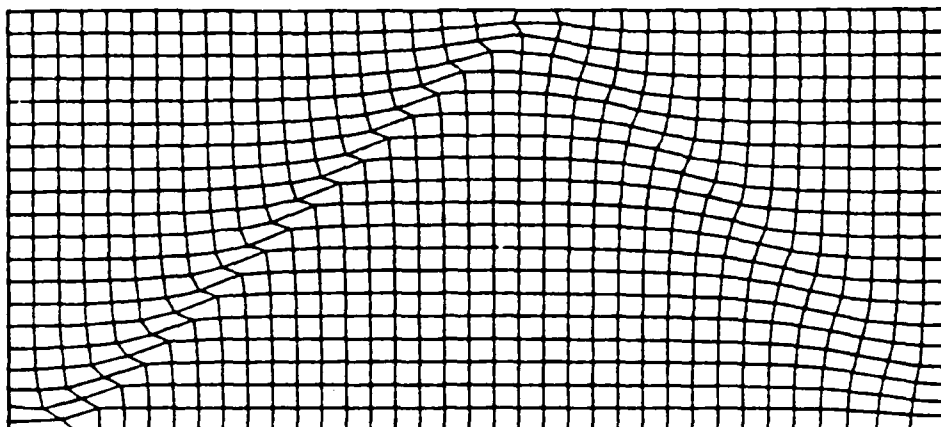


(a)

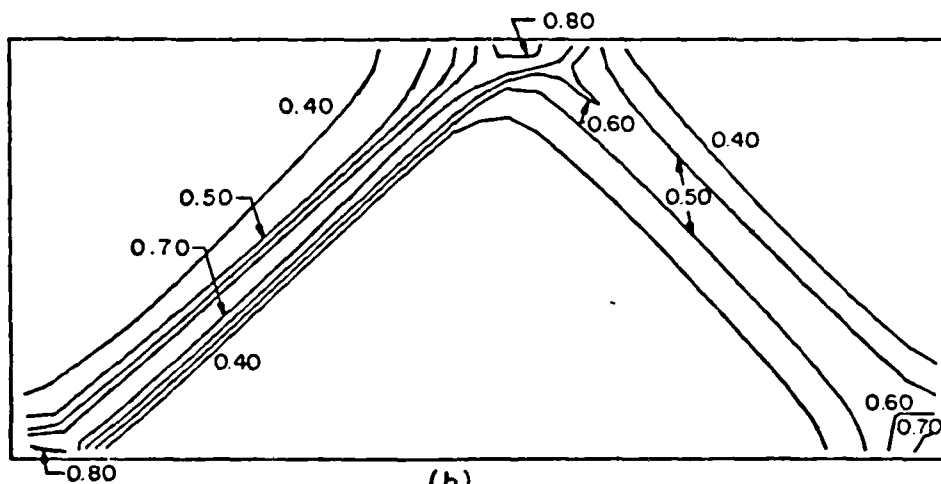


(b)

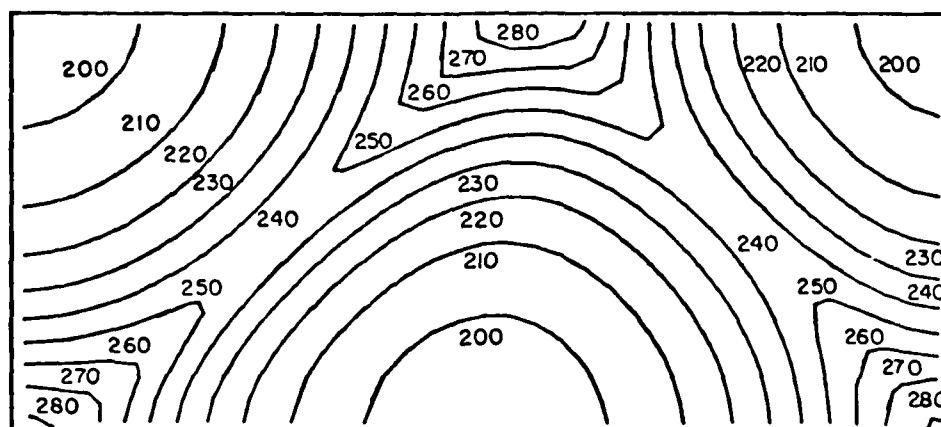
FIGURE 17



(a)

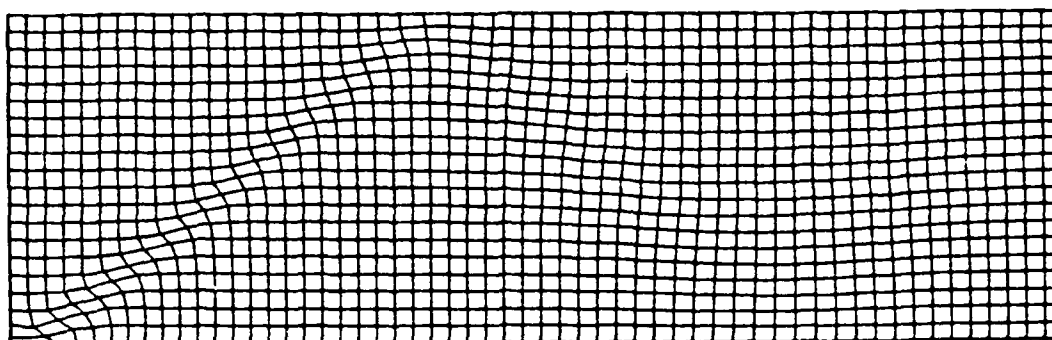


(b)

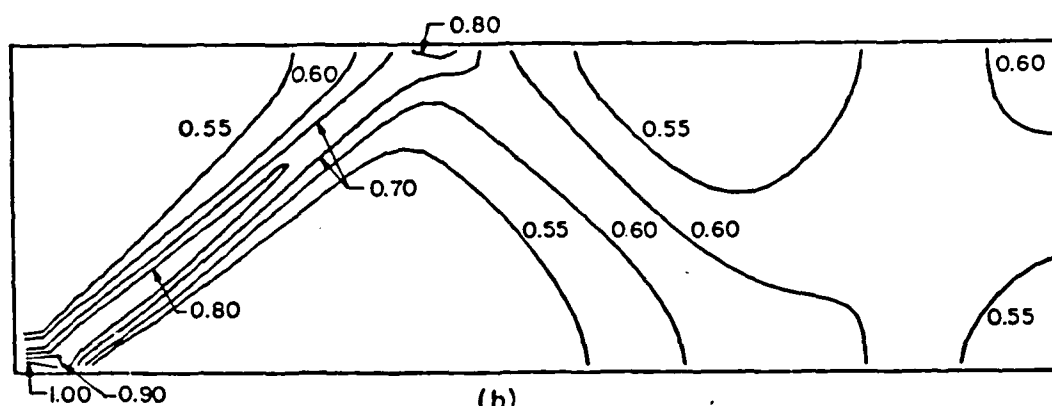


(c)

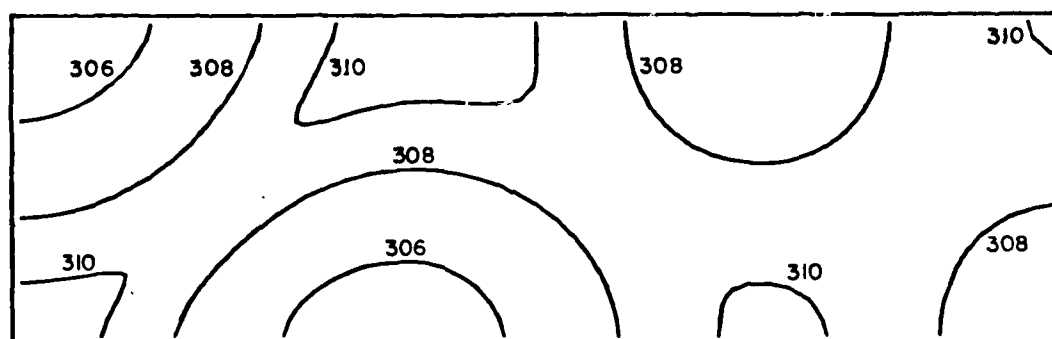
FIGURE 18



(a)



(b)



(c)

FIGURE 19

END

DTIC

7-86